

# Three-Dimensional NDE of VHTR Core Components via Simulation-Based Testing

---

## Reactor Concepts

Dr. Bojan Guzina

University of Minnesota

In collaboration with:

Idaho National Laboratory

William Corwin, Federal POC  
Dennis Kunerth, Technical POC

**FINAL REPORT**  
**NEUP Project 10-862**

**Three-dimensional NDE of VHTR core components  
via simulation-based testing**

**September 30, 2014**

**Abstract**

A next generation, simulation-driven-and-enabled testing platform is developed for the 3D detection and characterization of defects and damage in nuclear graphite and composite structures in Very High Temperature Reactors (VHTRs). The proposed work addresses the critical need for the development of high-fidelity Non-Destructive Examination (NDE) technologies for as-manufactured and replaceable in-service VHTR components. Centered around the novel use of elastic (sonic and ultrasonic) waves, this project deploys a robust, non-iterative inverse solution for the 3D defect reconstruction together with a non-contact, laser-based approach to the measurement of experimental waveforms in VHTR core components. In particular, this research (1) deploys three-dimensional Scanning Laser Doppler Vibrometry (3D SLDV) as a means to accurately and remotely measure 3D displacement waveforms over the accessible surface of a VHTR core component excited by mechanical vibratory source; (2) implements a powerful new inverse technique, based on the concept of Topological Sensitivity (TS), for non-iterative elastic waveform tomography of internal defects – that permits robust 3D detection, reconstruction and characterization of discrete damage (e.g. holes and fractures) in nuclear graphite from limited-aperture NDE measurements; (3) implements state-of-the-art computational (finite element) model that caters for accurately simulating elastic wave propagation in 3D blocks of nuclear graphite; (4) integrates the SLDV testing methodology with the TS imaging algorithm into a non-contact, high-fidelity NDE platform for the 3D reconstruction and characterization of defects and damage in VHTR core components; and (5) applies the proposed methodology to VHTR core component samples (both two- and three-dimensional) with a priori induced, discrete damage in the form of holes and fractures. Overall, the newly established SLDV-TS testing platform represents a next-generation NDE tool that surpasses all existing techniques for the 3D ultrasonic imaging of material damage from non-contact, limited-aperture waveform measurements.

**Outlook.** The next stage in the development of this technology includes items such as (a) non-contact generation of mechanical vibrations in VHTR components via thermal expansion created by high-intensity laser; (b) development and incorporation of Synthetic Aperture Focusing Technique (SAFT) for elevating the accuracy of 3D imaging in highly noisy environments with minimal accessible surface; (c) further analytical and computational developments to facilitate the reconstruction of diffuse damage (e.g. microcracks) in nuclear graphite as they lead to the dispersion of elastic waves, (d) concept of model updating for accurate tracking of the evolution of material damage via periodic inspections; (d) adoption of the Bayesian framework to obtain information on the certainty of obtained images; and (e) optimization of the computational scheme toward real-time, model-based imaging of damage in VHTR core components.

## Task 1: Manufacturing of damaged VHTR core components

As shown in Fig. 1, the damaged graphite specimens that were manufactured and tested during the course of this investigation include:

- Plate-1,  $364 \times 306 \times 20$  mm, damage: 25 mm through hole
- Plate-2,  $364 \times 306 \times 20$  mm, damage: 25 mm through hole and  $38 \text{ mm} \times 0.7 \text{ mm}$  hairline crack
- Block-1,  $364 \times 306 \times 172$  mm, damage:  $130 \times 26$  mm cylindrical cavity

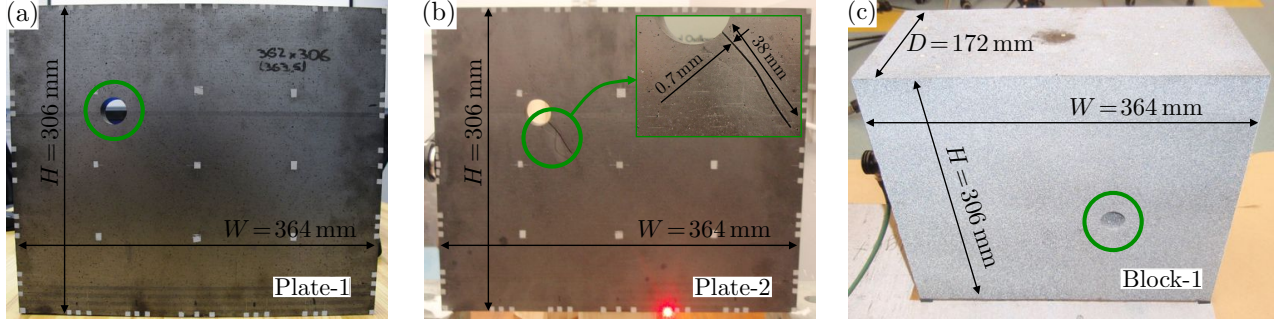


Figure 1: Damaged graphite specimens, note the Block-1 specimen was painted with retroreflective paint to enhance SLDV measurements.

Plate-1 was manufactured for an initial demonstration test dedicated to verifying the proposed approach for discrete damage imaging in nuclear graphite. Plate-2 specimen features an additional “crack-like” damage introduced at the circumference of the hole to simulate crack initiation under the load. Tests performed on this specimen were dedicated to verifying the capacity of the proposed NDE approach to *identify/image cracks* in graphite. Finally, Block-1 specimen was manufactured to check the method in a realistic 3D configuration with a *limited aperture* of illuminating sources/registering receivers.

In addition to creating discrete defects an attempt was made to induce diffuse damage via uniaxial loading of the plate specimen as shown in Fig. 2. Though in compression, the elastic solution for the circular opening in an infinite medium (see formula below) features the tensile stress  $-T$  when  $\theta = 0, \pi$  where crack initiation was expected. The process of loading was accompanied by recording the acoustic emission (AE) activity near the hole to confirm initiating of the micro cracks. With total of 4 sensors (attached to the back side of the plate) about 50 AE events were registered during incremental increase of the load up to 18.5 MPa, however, no visible material deterioration was identified after the loading was discontinued, see the display.

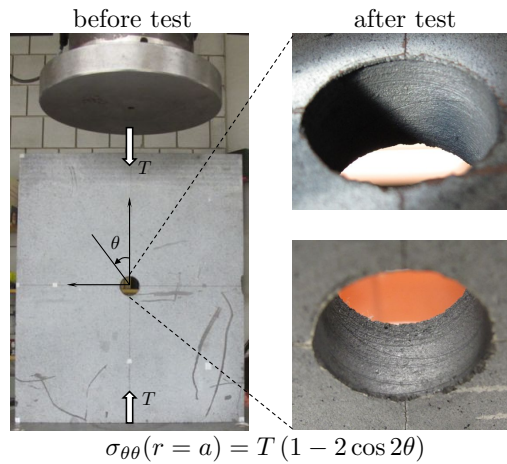


Figure 2: Uniaxial loading test of the plate specimen.

## Task 2: CT scanning of damaged VHTR core components

In this task an auxiliary graphite block ( $187 \times 55 \times 68$  mm) shown in Fig. 3 was scanned via micro-computed tomography (CT) in order to determine the density distribution from the reconstructed 3D images.

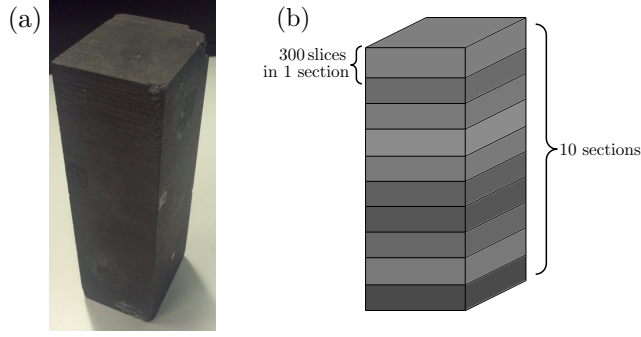


Figure 3: Graphite block scanned and analyzed using micro-CT: (a) photograph of the block, (b) schematic diagram showing the division of the graphite block into 10 sections with 300 CT slices in each section.

### Methods

The block in Fig. 3a was scanned a high-resolution micro-CT system [2]. The CT parameters used in the scanning were: 120 kV voltage,  $221 \mu\text{A}$ ,  $33 \mu\text{m}$  resolution, 1080 projections and 4 frames/projection. The software ImageJ [1] was used for performing the analysis of the CT images. The gray values ( $g$ ) were converted to densities ( $\rho$ ) assuming a linear relationship, with the minimum gray value representing a void in the block, i.e. zero density, and the maximum gray value representing the maximum density region in the graphite:

$$g_{\min} \rightarrow \rho = 0 \text{ g/cm}^3 \quad (1)$$

$$g_{\max} \rightarrow \rho = \rho_{\max} = 2.27 \text{ g/cm}^3 \quad (2)$$

The relation between the density and the gray value is given as:

$$\rho = \frac{\rho_{\max}}{g_{\max} - g_{\min}} (g - g_{\min}) \quad (3)$$

The maximum density of the graphite  $\rho_{\max} = 2.27 \text{ g/cm}^3$  is based on the theoretical value for defect-free graphite [17]. The CT images contained a number of voxels with very high gray vales. These were thought to be non-graphite impurities with high atomic numbers, or electronic noises from the X-ray detectors. Thus, the maximum gray value for defect-free graphite  $g_{\max}$  was obtained by calibration using the following relation:

$$\bar{\rho} = \frac{\rho_{\max}}{g_{\max} - g_{\min}} (\bar{g} - g_{\min}), \quad (4)$$

where  $\bar{\rho}$  is the mean density (measured at  $1.85 \text{ g/cm}^3$ ) and  $\bar{g}$  is the mean gray value of the micro-CT image of the entire graphite block. The porosity  $p$  was calculated using the following expression:

$$p = 1 - \frac{\bar{\rho}}{\rho_{\max}}$$

Figure 3b shows a schematic diagram of the graphite block divided into 10 sections, with each section being comprised of 300 slices. For each of the sections, the gray value distribution and the mean density was determined using (4). Figure 4a shows the 3D CT reconstruction of the graphite block and Figure 4b shows the region of interest selected in the CT image for performing the analysis.

### Results

Figure 5 shows the gray value distribution (pixel count vs. gray value) for a section of the graphite block. The minimum  $g_{\min}$  and maximum  $g_{\max}$  gray values were determined to be 12334 and 17600 respectively. Figure 6 shows the variations of mass density and porosity in the graphite block with height. It can be seen that there is a small gradual reduction in density towards the mid-height of the block.



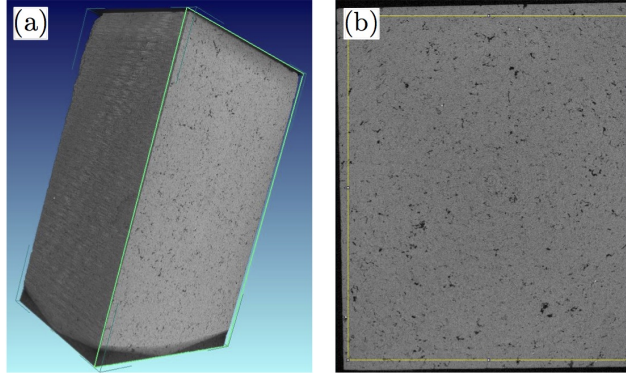


Figure 4: CT reconstruction of the graphite block: (a) full 3D reconstruction picture, (b) region of interest (yellow rectangle) for performing the analysis of the CT image.

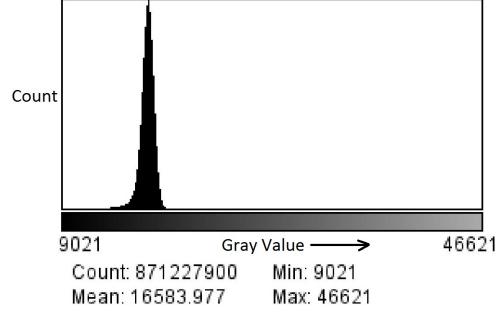


Figure 5: Gray value histogram for CT images in a section of the graphite block.

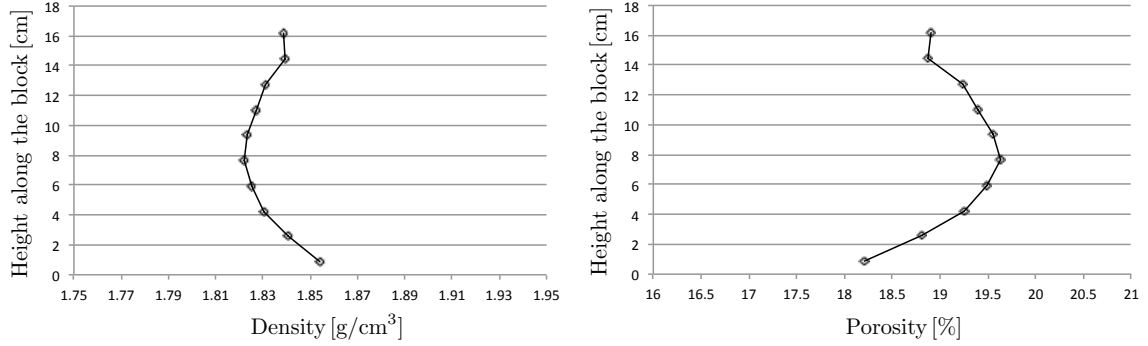


Figure 6: Density profiles of the graphite block measured along the vertical direction in Fig. 3 in terms of: mass density (left panel), and porosity (right panel).

### Task 3: Inverse solution for 3D imaging and characterization of damage

Over the past decade, the method of Topological Sensitivity (TS) has been shown to provide a simple non-iterative approach to the wave-based imaging of defects in elastic media. Its strength lies in providing a computationally efficient and robust way of identifying and geometrically reconstructing distinct inner heterogeneities (inclusions, voids, or cracks) without the need for prior information in the form of initial guess. This task is an account of the results obtained, i) by generalizing TS method for the reconstruction of partially closed cracks in elastodynamics, and, ii) by analyzing TS for the imaging of impenetrable (Dirichlet and Neumann) obstacles in the high-frequency regime leading to a new reconstruction logic.

#### Ultrasonic imaging of discrete fractures

In this section, the capability of TS in determining the contact condition between the surfaces of a crack embedded in an elastic medium is investigated, where a schematic illustration of this problem is provided in Fig. 7. To this end, the inverse scattering of time-harmonic elastic waves by a smooth arbitrary-shaped crack

$\Gamma \subset \mathcal{B}_1 \subset \mathbb{R}^3$ , is considered, where the contact condition at the interface  $\Gamma^\pm$  may vary e.g. be partially closed (due to surface asperities), fluid filled, or traction free. It should be mentioned,  $\mathcal{B}_1$  represents the sampling region i.e. search area for the hidden crack. For the sake of brevity, in the following analysis we consider the canonical case of illuminating the hidden crack in  $\mathbb{R}^3$  by the plane incident wave  $\mathbf{u}^i$ ; The action of which on  $\Gamma$  results in the scattered field  $\tilde{\mathbf{u}}$  observed in the form of

$$\mathbf{u}(\boldsymbol{\xi}) = \mathbf{u}^i(\boldsymbol{\xi}) + \tilde{\mathbf{u}}(\boldsymbol{\xi}), \quad \boldsymbol{\xi} \in \mathbb{R}^3 \setminus \Gamma$$

known as the total field over a closed measurement surface  $\Gamma^{\text{obs}}$ . The reference medium is assumed to be linear, elastic, isotropic and homogeneous which is characterized by mass density  $\rho$ , shear modulus  $\mu$  and Poisson's ratio  $\nu$ . In this setting, the scattered field  $\tilde{\mathbf{u}}$  described by the following differential equation and its associated boundary condition,

$$\nabla \cdot [\mathbf{C} : \nabla \tilde{\mathbf{u}}](\boldsymbol{\xi}) + \rho \omega^2 \tilde{\mathbf{u}}(\boldsymbol{\xi}) = \mathbf{0}, \quad \boldsymbol{\xi} \in \mathbb{R}^3 \setminus \Gamma \quad (5)$$

$$\mathbf{t}^\pm[\tilde{\mathbf{u}}](\boldsymbol{\xi}) = \mp \mathbf{K}[\tilde{\mathbf{u}}](\boldsymbol{\xi}) - \mathbf{t}_f^\pm, \quad \boldsymbol{\xi} \in \Gamma^\pm. \quad (6)$$

where  $[\tilde{\mathbf{u}}] = \tilde{\mathbf{u}}^+ - \tilde{\mathbf{u}}^-$  is the crack opening displacement (COD) and,  $\mathbf{C}$  is the fourth-order elasticity tensor. The effect of micro asperities can be considered as arbitrary spatial distributions of linear springs in both normal and tangential directions described by a second-order, symmetric and positive definite stiffness tensor  $\mathbf{K}(\boldsymbol{\xi})$ . In this study, the crack contact condition is modeled in the average sense, so that the stiffness matrix is constant i.e.  $\mathbf{K}(\boldsymbol{\xi}) = \mathbf{K}$ .

The cost functional for the TS analysis is least-squares based, and its first variation is asymptotically calculated for the nucleation of an infinitesimal penny-shaped crack endowed with an arbitrary set of (normal and tangential) constant interfacial stiffnesses, represented as the trial stiffness matrix  $\mathbf{K}_t$  (see Fig. 7). The resulting TS expression reads as the following,

$$\mathbf{T}(\boldsymbol{\xi}, \mathbf{K}_t) = \boldsymbol{\sigma}(\boldsymbol{\xi}) : \mathbf{A} : \hat{\boldsymbol{\sigma}}(\boldsymbol{\xi}), \quad (7)$$

where  $\boldsymbol{\sigma}$  and  $\hat{\boldsymbol{\sigma}}$  are two forward solutions for the reference domain, namely the incident field and the so-called adjoint field (see [e.g. 13]). The elastic polarization tensor  $\mathbf{A}$  is computed, via the dimensional analysis, in terms of a suitable elastostatic solution for a unit crack with interfacial stiffness in  $\mathbb{R}^3$  that is subjected to constant stresses at infinity, and, can be expressed as follows

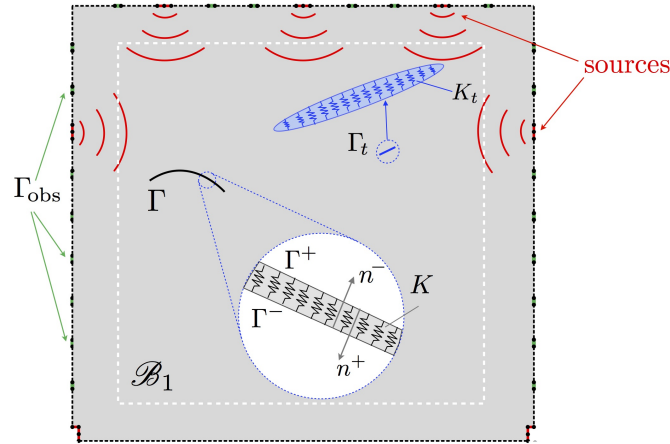


Figure 7: Arbitrarily shaped crack with interfacial stiffness illuminated by elastic waves.

$$\mathbf{A}(\mu, \nu, \mathbf{K}_t) = \alpha_s (\mathbf{n} \otimes \mathbf{e}_\beta + \mathbf{e}_\beta \otimes \mathbf{n}) \otimes (\mathbf{n} \otimes \mathbf{e}_\beta + \mathbf{e}_\beta \otimes \mathbf{n}) + \alpha_n (\mathbf{n} \otimes \mathbf{n} \otimes \mathbf{n} \otimes \mathbf{n}), \quad \beta = 1, 2, \quad (8)$$

where

$$\alpha_s = \frac{4}{3\mu(2-\nu)} \frac{1-\nu^2}{k_s + \nu + 1}, \quad \alpha_n = \frac{8(1-\nu)}{3\mu} \frac{2\nu + 1}{k_n + 2\nu + 1},$$

and  $k_s$  and  $k_n$  are the trial shear and normal stiffness respectively i.e.  $\mathbf{K}_t = k_n(\mathbf{n} \otimes \mathbf{n}) + k_s(\mathbf{e}_\beta \otimes \mathbf{e}_\beta)$ ,  $\beta = 1, 2$ .  $\mathbf{n}$  is the trial crack normal vector and  $\mathbf{e}_\beta$  with  $\beta = 1, 2$  are the corresponding tangential directions. With such mathematical result, a computational platform based on the regularized boundary integral equation method

for 3D elastodynamics is developed to simulate the experimental data and calculate the TS field over a range of testing frequencies. Reconstructions based on the new TS formula shows that the location and normal vector to the surface of a finite crack with interfacial stiffness are identifiable irrespective of the contact condition. Fig. 8 shows the TS reconstruction of a partially closed penny shaped crack and its associated normal vector. The crack is illuminated by sixteen low-frequency incident plane waves all around the unit sphere of incident directions. It should be mentioned, the procedure takes advantage of the full aperture of measurements. The true values of parameters are  $\mu=1$ ,  $\nu=0.35$  and  $k_s=k_n=3$ , while the trial crack is traction free i.e. the trial contact variables are  $k_s=k_n=0$ .

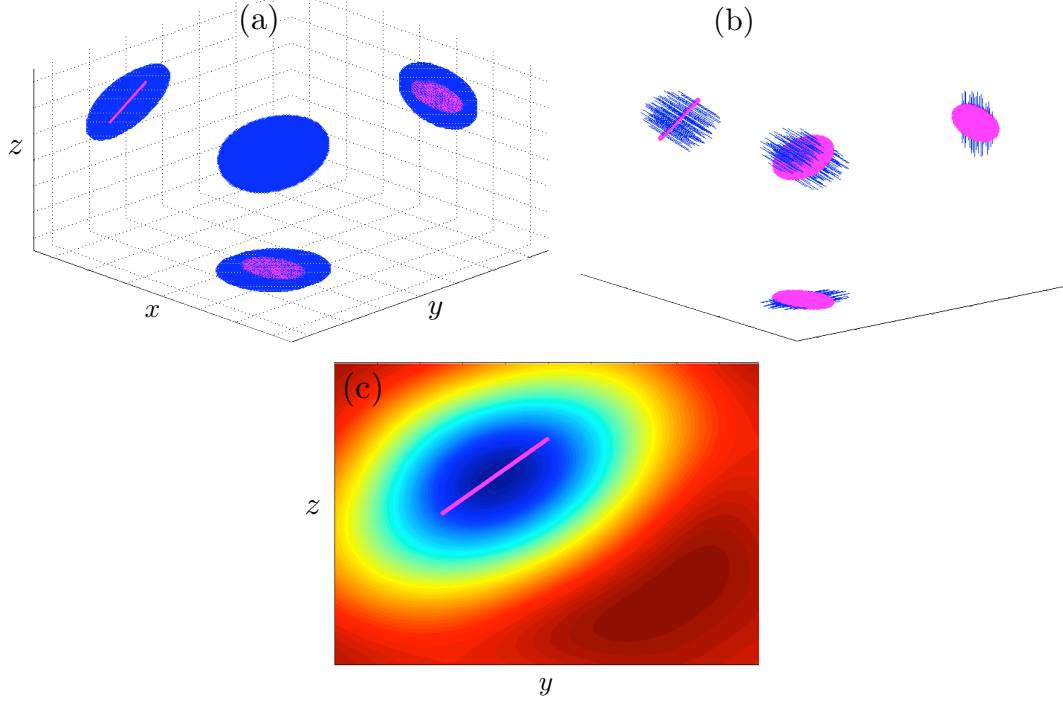


Figure 8: Reconstruction of a crack with interfacial stiffness, (a) three-dimensional representation of the true crack (pink) and the truncated TS field (blue) (b) the identified normal vector of the crack (c) TS distribution in the mid-section of the crack.

Having this initial information about the hidden crack, it is shown mathematically that useful information about the crack interface can further be extracted non-iteratively from the two independent terms featured in the newly obtained TS formula,

$$T(\xi, k_n, k_s) = -(\alpha_n^{\text{true}} \alpha_n^{\text{trial}} T_1 + \alpha_s^{\text{true}} \alpha_s^{\text{trial}} T_2), \quad (9)$$

one is related to the normal crack stiffness and the other to its tangential counterpart.  $T_1$  and  $T_2$  in Eq. (9) are related to Stokes fundamental solution and the free field stress distribution. Given this new interpretation, one can qualitatively identify the interfacial condition – in the low-frequency regime – by comparing two different TS distributions corresponding to the following trial contact parameters, i)  $k_n = 0$ ,  $k_s \rightarrow \infty$ , and ii)  $k_n \rightarrow \infty$ ,  $k_s = 0$ . The TS field experiencing the highest negative values (at the crack location) is affiliated with the direction of the smallest interfacial stiffness (of the *true* crack). Fig. 9 illustrates the effectiveness of this approach where the two fields  $T(\xi, 0, 50)$  and  $T(\xi, 50, 0)$  in the mid-section of the crack – whose the geometry is shown in Fig. 8 (a) – are computed and compared for several contact situations i.e. when the *true* crack is traction free, fluid filled and when  $k_n \ll k_s$ . From Fig. 9, one can clearly distinguish these contact conditions from one another.

It is worth noting, in the case where similar situation prevails in both directions (normal and tangential), e.g. the traction free case, the contribution of both terms in Eq. (9) to the final TS field is of the same order.

With reference to Fig. 10 (where the true scatterer is a cylindrical crack), as the frequency of the illuminating plane wave increases, the maximum negative TS values localize around the crack boundary which reveals the shape reconstruction capability of topological sensitivity in the medium to high-frequency regime.

Fig. 11 represents the three-dimensional truncated TS reconstruction along with its distribution in the mid-section of a penny shaped crack in the high frequency regime, where the illuminating wavelength is one

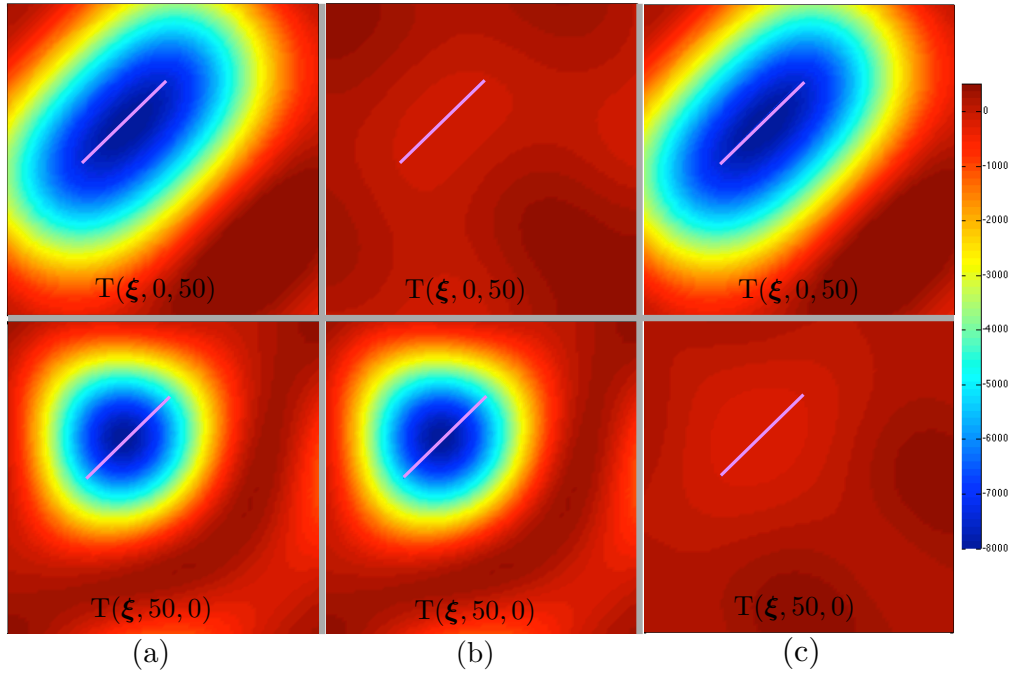


Figure 9:  $T_1$  and  $T_2$  distributions when the true crack is (a) traction free in both directions  $k_s = k_n = 0$ , (b) fluid-filled (true  $k_s \ll k_n$ ), (c) the true normal stiffness is much smaller than the shear stiffness  $k_n \ll k_s$ .

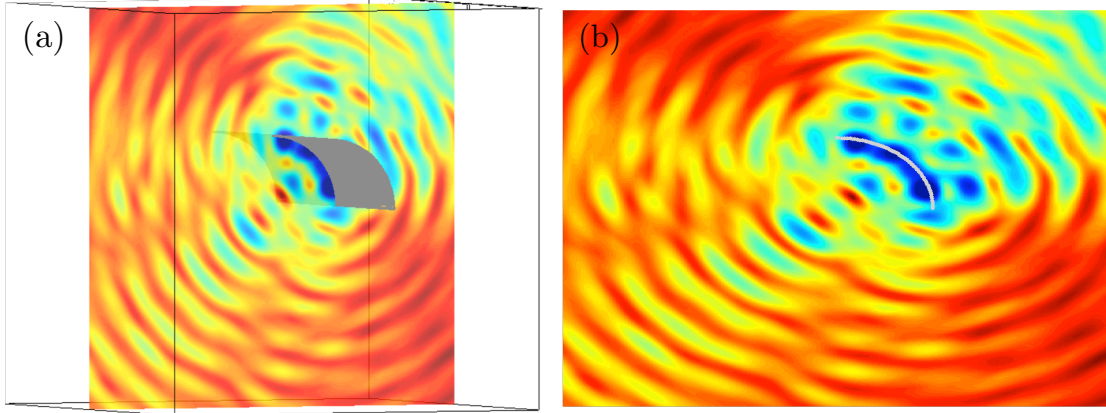


Figure 10: TS reconstruction of a cylindrical crack, (a) the true crack (gray) (b) TS field in the crack mid-section.

half of the crack diameter. The true crack in Fig. 11 (a) and (b) is traction free, while the contact parameters in (c) and (d) are  $k_n = k_s = 6$ . It appears that the TS behavior in high frequencies has a strong correlation with the interfacial condition such that in the traction free case, the TS successfully reconstructs the crack tip profile while in the case of partially closed crack, its surface is identified. This case is currently under further investigations. As the first step toward understanding the TS high-frequency behavior, next section analyzes anomaly reconstruction via topological sensitivity in acoustic scattering.

As a concluding remark it should be mentioned that the results obtained extend naturally to finite bodies and other types of excitation, e.g. piezoelectric sources on the boundary (see [26]).

## High-frequency imaging of material defects and damage by topological sensitivity

While testing nuclear graphite specimens at higher excitation frequencies where the illuminating (shear) wavelength is smaller than characteristic defect size, it was found that the topological sensitivity (TS) does not follow the expected behavior in that it *does not attain* pronounced negative values *inside* a material defect. This is illustrated in Fig. 12 which plots the distribution of TS in an aluminum plate at 40 kHz (left panel) and that in a solid block of nuclear graphite at 30 kHz (right panel). As can be seen from the display, the TS

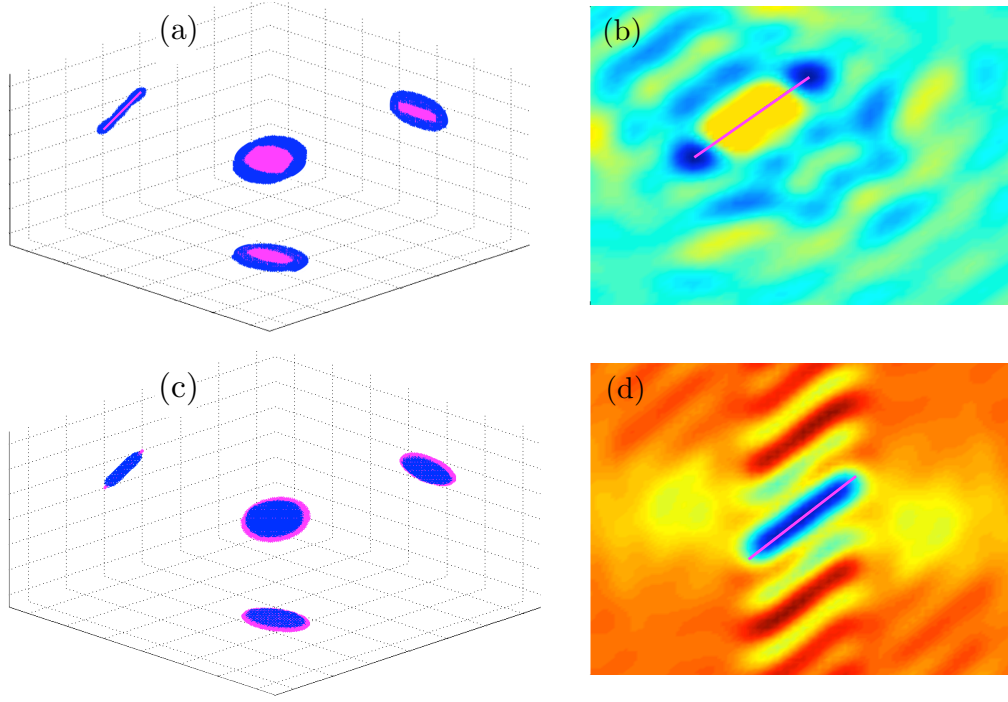


Figure 11: High-frequency behavior of the TS reconstruction in the case of traction free, (a),(b) and partially closed (c),(d) cracks.

in such cases traces the *the boundary of a defect* rather than filling its *interior*. Motivated by this observation, an effort was made to understand this behavior toward the quality assurance (QA) of damage characterization and imaging by topological sensitivity.

To this end, the topological sensitivity is considered in the context of Helmholtz equation for imaging anomalies in the high-frequency regime, where the germane wavelength is surpassed by the remaining length scales in the problem.

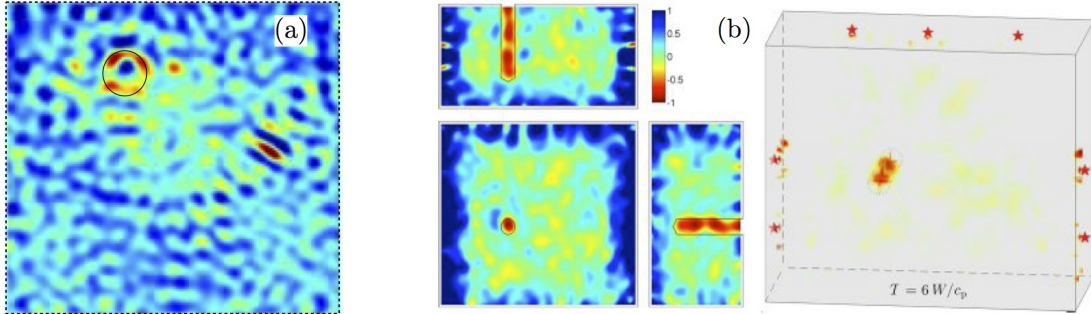


Figure 12: the distribution of TS using experimental data, (a) in an aluminum plate at 40 kHz (left panel) and, (b) in a solid block of nuclear graphite at 30 kHz (right panel).

It is assumed that the hidden obstacle  $D$  is convex and impenetrable, and that the measurements of the scattered field are taken over a sphere whose radius is large relative to the size of the interrogated region. In this setting, the formula for topological sensitivity – which quantifies the perturbation of a cost functional due to introduction of a point-like scatterer – is expressed as a pair of nested surface integrals: one taken over the boundary of a hidden obstacle, and the other over the measurement surface. Using multipole expansion, the latter integral is reduced to a set of antilinear forms featuring the Green’s function and its gradient. The remaining expression is distilled by evaluating the scattered field on the surface of an obstacle via Kirchhoff approximation [5], and pursuing the asymptotic expansion of the remaining Fourier integral. In this way the topological sensitivity is found to survive upon three asymptotic lynchpins, namely i) the near-boundary approximation for sampling points close to the “exposed” surface of an obstacle; ii) uniform expansions synthesizing the diffraction catastrophes for sampling points near caustic surfaces, lines, and points; and



iii) non-uniform (stationary phase) approximation. Within the framework of the catastrophe theory [4, 23, 25, 6] it is shown that, in the case of the full source aperture, the topological sensitivity is asymptotically dominated by the (explicit) near-boundary term,

$$T(\xi, \beta, \gamma) \simeq \delta \frac{\pi k}{(k\ell)^3} \left\{ \frac{3(1-\beta)}{2+\beta} (k\ell \cos(k\ell) - \sin(k\ell))^2 - (1-\beta\gamma^2) (k\ell)^2 \sin(k\ell)^2 \right\} \quad d(\xi, D) \leq \frac{2\pi}{k}, \quad (10)$$

where  $\delta = +1, -1$  respectively for Dirichlet and Neumann obstacles.  $k$  stands for the illuminating wave number and  $\ell$  denotes the normal distance of the sampling point  $\xi$  to the scatterer  $D$ . Moreover,  $\beta = \rho/\rho_{\text{trial}}$  and  $\gamma = c/c_{\text{trial}}$  synthesize the material characteristics of a *trial obstacle*. For the complete account of the proof see [14]. Eq. (10) explains the previously reported reconstruction capabilities (e.g. see [7, 11]) and the experimental observations in Fig. 12. This result further unveils the new reconstruction logic at short wavelengths where the boundary of an anomaly is obtained as a zero level set of the TS field separating its extreme negative and extreme positive values.

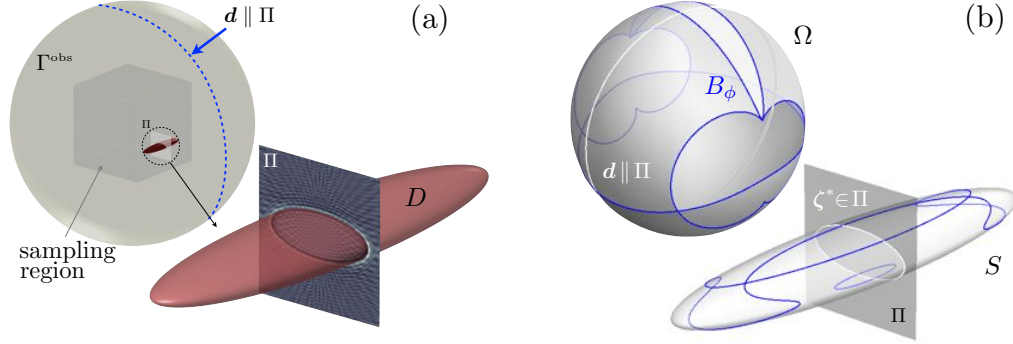


Figure 13: (a) sensing configuration, and (b) bifurcation set  $B_\phi(\mathbf{d}, \xi) \subset \Omega$  with affiliated critical points  $\zeta^* \in S$  (dark curves) for one sampling point. Loci  $\mathbf{d} \parallel \Pi$  and matching  $\zeta^*$  are shown in white (see [14]).

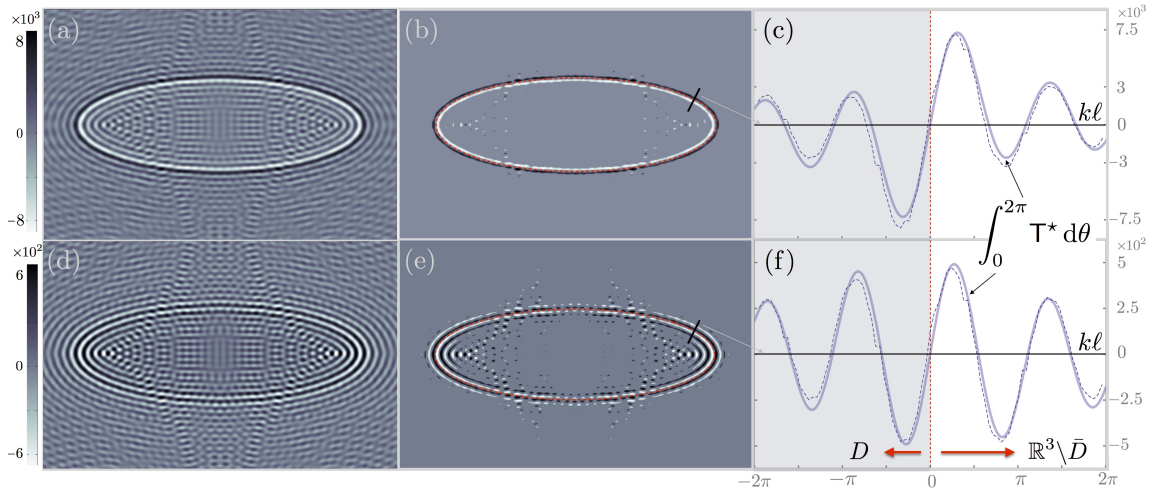


Figure 14: Distribution of  $T_\Pi(\xi, \beta, \gamma)$  for a Dirichlet obstacle probed by  $(\beta = 20, \gamma = 1)$  (top row), and Neumann obstacle sampled by  $(\beta = 0, \gamma)$  (bottom row): full variation (left), thresholded distribution (middle), and example near-boundary variation (right). The thin dashed line in panels (b) and (e) traces  $S \cap \Pi$ .

A numerical experiment is devised to illustrate the performance of TS in the high-frequency regime. The sensing arrangement is shown in Fig. 13 (a) where  $D$  is an ellipsoidal anomaly with semi-axes  $(0.2, 0.08, 0.8)$  and boundary  $S$ . The TS distribution is computed in the obstacle's mid-section  $\Pi$  perpendicular to its major axis, assuming incident plane waves with  $k = 300$  (wavelength  $\lambda = 0.021$ ) propagating in direction  $\mathbf{d} \parallel \Pi$ . It is noted that the ellipsoid's minimum radius of curvature is  $0.032 \sim 1.5\lambda$ .

The reconstruction of a Dirichlet obstacle via  $T_\Pi(\xi, 20, 1)$  is compared in Fig. 14 to that of a Neumann anomaly by  $T_\Pi(\xi, 0, \gamma)$ . Here the left, middle, and right panels plot respectively  $T_\Pi$ , thresholded  $T_\Pi$ , and example near-boundary variation of  $T_\Pi$  (along the indicated normal) versus the asymptotically dominated contribution reported in Eq. (10).

For the sake of completeness, the high-frequency reconstruction of an onion-shaped (non-symmetric) material defect by TS is shown in Fig. 16 where the full 3D source aperture is the unit sphere. The reconstructed obstacle and its projections are shown in dark blue, while the contours enclosing the boundary of the *true* scatterer is displayed in bright blue i.e. cyan on the sides for comparison.

To conclude this section, the new algorithm is applied to identify the boundary of a circular hole in an aluminum plate from the recent set of *elastodynamic* experiments [26]. In this case the wave motion, governed by the two-dimensional Navier equations, is induced in a *bounded* domain shown in Fig. 15(a) and monitored along its top and side edges. The incident waves are generated by a piezoelectric transducer, placed sequentially at five locations indicated in the diagram, such that the ratio of the illuminating wavelength to the hole diameter is 0.85. Thus, the testing configuration is incompatible with the present analysis in several aspects, including (i) dimensionality of the problem, (ii) type of the governing equation, (iii) geometry of the anomaly-free domain, (iv) probing wavelength, and (v) aperture of the illuminating sources. Nonetheless the reconstruction of a circular hole in panel (c), obtained by applying the new logic to the TS distribution [26] showing in panel (b), is rather satisfactory.

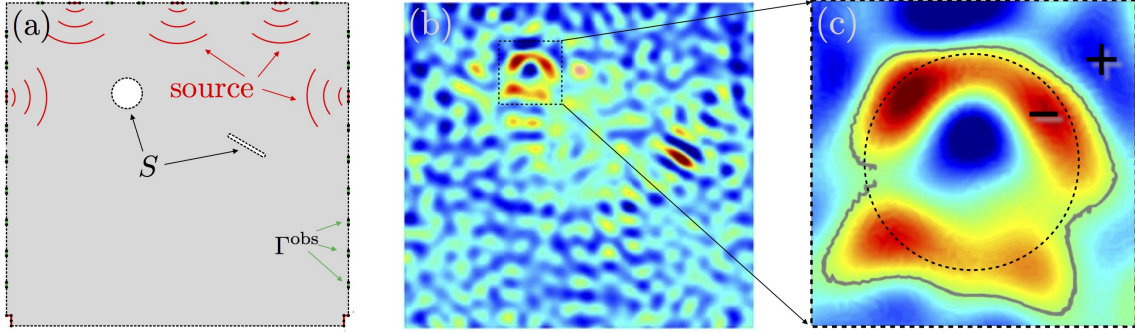


Figure 15: Elastodynamic experiment in [26]: (a) testing setup, (b) five-sources TS field, and (c) true boundary (dashed circle) versus its reconstruction (solid irregular line) obtained via Algorithm 1.

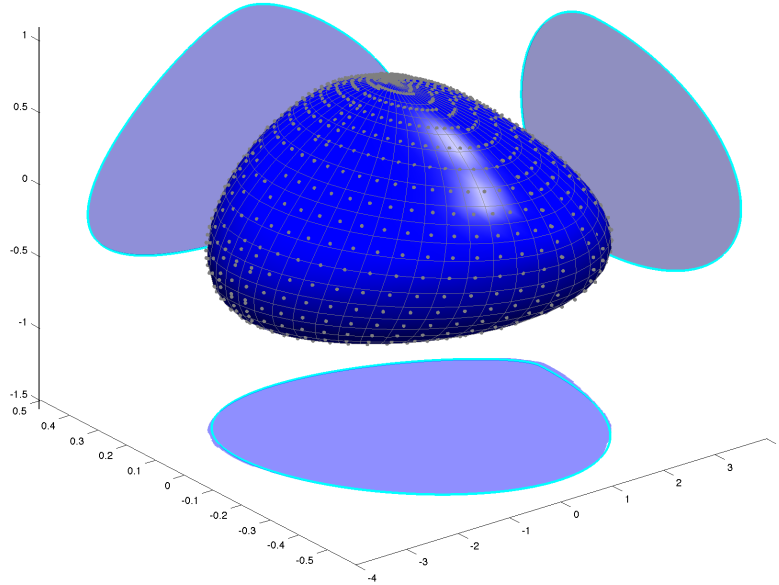


Figure 16: 3D high-frequency reconstruction of an onion-shaped material defect by Topological Sensitivity.



## Task 4: 3D simulation of the SLDV experiments

Based on the observations in Task 2 and Task 7, the intact nuclear graphite can be modeled as an isotropic and homogeneous elastodynamic medium characterized by Young's modulus  $E$ , Poisson's ratio  $\nu$ , or the corresponding Lamé constants  $\lambda = \frac{E\nu}{(1+\nu)(1-2\nu)}$ ,  $\mu = \frac{E}{2(1+\nu)}$ , and mass density  $\rho$ . Assuming no body forces arise in the graphite, a transient elastodynamic problem is defined over domain  $\Omega \times [0, T]$  through the system of Navier equations:

$$\begin{aligned} \nabla \cdot (\mathbf{C} : \nabla \mathbf{u}) (\boldsymbol{\xi}, t) &= \rho \ddot{\mathbf{u}}(\boldsymbol{\xi}, t), & (\boldsymbol{\xi}, t) &\in \Omega \times [0, T], \\ \mathbf{n} \cdot \boldsymbol{\sigma} &= \mathbf{t}^*, & (\boldsymbol{\xi}, t) &\in \Gamma^N \times [0, T], \\ \mathbf{u} &= \mathbf{u}^*, & (\boldsymbol{\xi}, t) &\in \Gamma^D \times [0, T], \\ \mathbf{u} = \dot{\mathbf{u}} &= 0, & \boldsymbol{\xi} \in \Omega, t &= 0, \end{aligned} \quad (11)$$

where  $\mathbf{C} = \lambda \mathbf{I}_2 \otimes \mathbf{I}_2 + 2\mu \mathbf{I}_4^{\text{sym}}$  is elastic stiffness tensor with  $\mathbf{I}_4^{\text{sym}}$  and  $\mathbf{I}_2$ , respectively, denoting the symmetric fourth-order and the second-order identity tensors. In this setting, the boundary of the domain  $\partial\Omega$  is split into Dirichlet  $\Gamma^D$  and Neumann  $\Gamma^N$  parts such that  $\partial\Omega = \Gamma^N \cup \Gamma^D$ ,  $\Gamma^N \cap \Gamma^D = \emptyset$ . An initial boundary value problem defined via (11) needs to be solved numerically twice with corresponding boundary conditions to obtain the free and adjoint states, which can be computationally expensive in a 3D setting. However, for the plate specimens Plate-1 and Plate-2 a plane stress assumption can be employed, in which a 3D problem is effectively reduced to a 2D problem with the Young's modulus  $E$  and Poisson's ratio  $\nu$  replaced by their corresponding effective values  $E'$  and  $\nu'$  [20]:

$$\nu' = \frac{\nu}{1 + \nu} \quad E' = E(1 - \nu'^2) \quad (12)$$

The validity of the plane stress assumption can be judged via the frequency content of the propagating waves [26], namely the dominant observed wavelength must be significantly larger than the plate thickness (in this case  $d = 20$  mm). At this stage, however, it was assumed that the plate specimens can be modeled within the plane stress approximation, as opposed to the three-dimensional configuration of the block specimen. As for choosing appropriate boundary conditions, at this stage it is assumed that in a SLDV experiment dynamic excitation is effected via contact piezo-ceramic transducer whose impact on the graphite specimen can be modeled via corresponding Dirichlet boundary condition, while the rest of the specimen's surface is assumed traction-free, see further clarification in Task 8.

The numerical scheme chosen for solving (11) is a conventional FE method coupled with unconditionally-stable Newmark scheme ( $\beta = 0.25$ ,  $\gamma = 0.5$ ). To reduce the cost of the simulations (especially in 3D), linear elements were implemented, commonly known as constant-strain triangle (CST) elements (constant-strain tetrahedron in 3D). To diminish the effects of numerical anisotropy and dispersion, dense unstructured meshes featuring at least 12 elements per p-wavelength were employed, such that  $\kappa = \frac{c_p}{f_c h_{\max}} \geq 12$ , where  $h_{\max}$  is the maximum distance between the nodes of the mesh, and  $f_c$  is the center frequency of the excitation wavelet, see Task 6. For example, Fig. 17 shows the meshes generated for FE simulations of the  $f_c = 30$  kHz wavefields featuring  $\kappa = 15.1, 22.1, 13.8$ , respectively, for Plate-1, Plate-2, and Block-1 specimens. Note also that for Plate-2 specimen the hole was included in the reference model to focus the reconstruction on imaging the crack alone. In the generated meshes, additional nodes were also added to specific points on the surface of the domain that correspond to the location of the scan points during subsequent SLDV testing to reduce the effort of interpolating the input data. In case of 2D triangular meshes a simple MATLAB-implemented mesh generator was utilized, while for 3D tetrahedron meshes an external package TetGen was employed. Following [26], the time step  $\Delta t$  of Newmark time integration was selected such that  $\frac{h_{\max}}{c_p \Delta t} = 1.45$ , while the duration of simulations  $T = N \Delta t$ , where  $N$  is the required number of time steps, was conveniently measured in terms of  $\tau = W/c_p$  – characteristic time required for a p-wave to travel the largest dimension of the specimen. For example, evaluation of the free field state arising in Block-1 specimen excited at  $f_c = 30$  kHz within the duration  $T = 6\tau$  requires  $N = 480$  time steps. For illustration, Fig. 18 shows the snapshots captured at  $t = 1.07\tau$  of the horizontal velocity component  $v_1$  of the free field wavefields obtained at  $f_c = 30$  kHz. Similarly, Fig. 19 shows snapshots of the adjoint field velocities  $\hat{v}_1$  captured at  $t = 1.2\tau$ .

As for FEM implementation, two different C++-based open source FE software packages were employed: initially FreeFEM++ [24] was used, later replaced by FEniCS package [21]. Switching from FreeFEM++ to FEniCS for both 2D and 3D simulations is advantageous in many ways. Developed by mathematical society, FEniCS has better support in terms of preconditioners/linear solvers and various types of the elements as compared to more “engineering” approach of FreeFEM++. Thus FEniCS is better suited for solving a large number of degrees of freedom system such as arising in a 3D elastodynamic problem of Block-1. Specifically, with the aid of built-in Jacobi preconditioner in FEniCS, inverting a  $10^5$ -DOF system with Conjugate Gradient

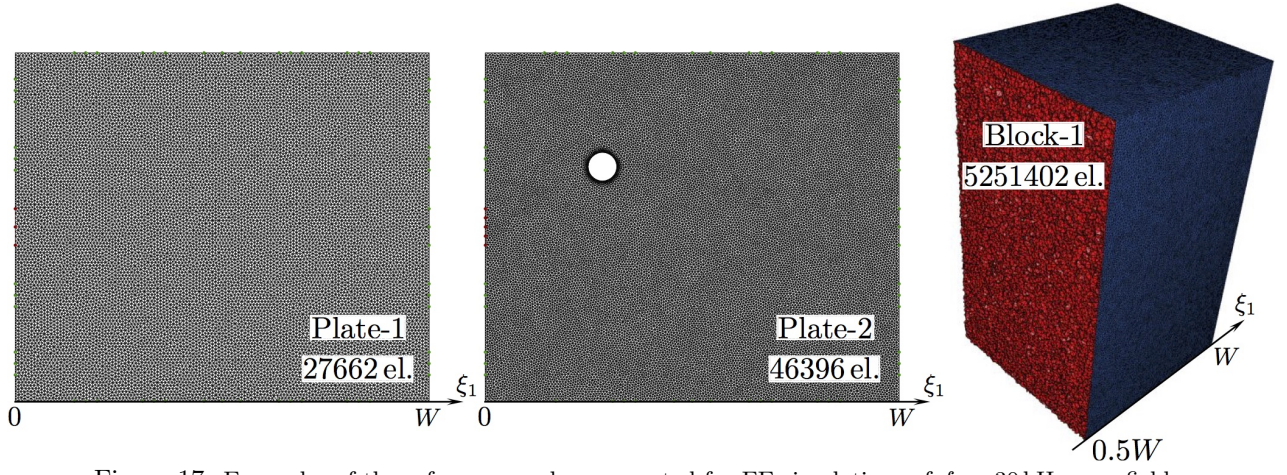


Figure 17: Examples of the reference meshes generated for FE simulations of  $f_c = 30$  kHz wavefields.

(CG) iterative solver is about 3 times faster compared to similar non-preconditioned solver in FreeFEM++. Also, since FEniCS is also available in Python, an efficient interface to MATLAB is provided via SciPy add-on which is especially helpful for storing and processing large FE/LDV data arrays.

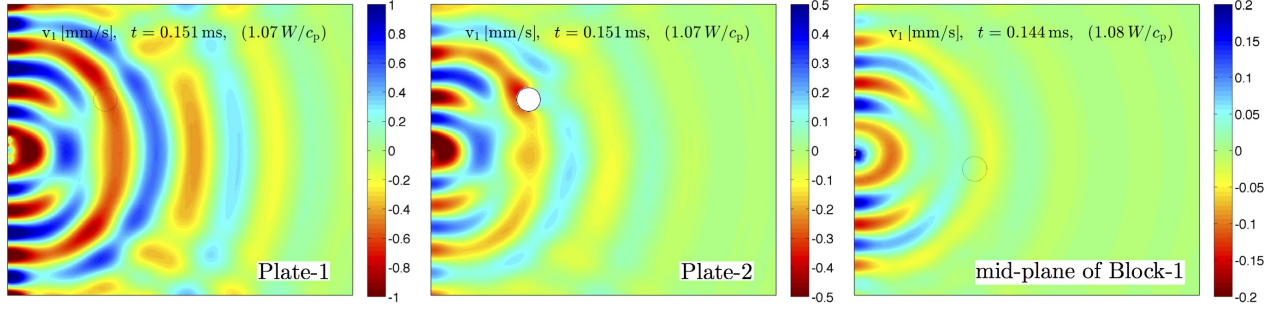


Figure 18: FE-simulated snapshots of  $v_1$  velocity component of the  $f_c = 30$  kHz *free* field wavefields.

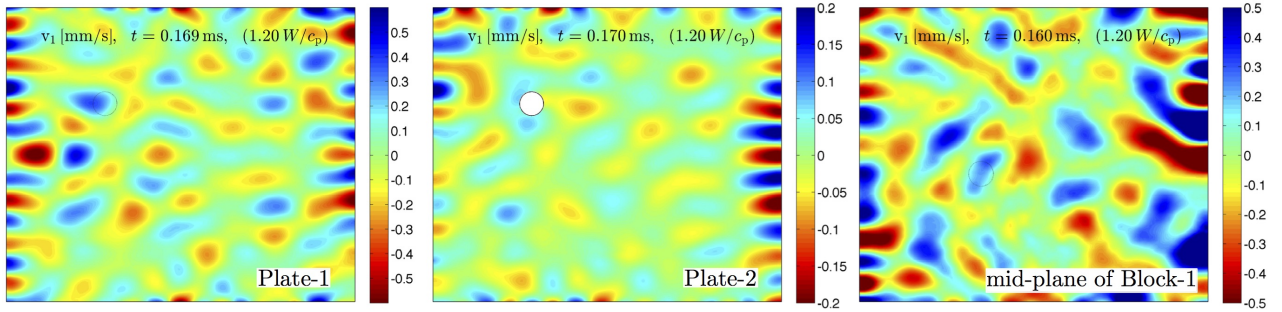


Figure 19: FE-simulated snapshots of  $\hat{v}_1$  velocity component of the  $f_c = 30$  kHz *adjoint* field wavefields.

## Task 5: Verification of the TS inverse solution using synthetic data

For the case of spherical or (respectively, circular) discrete cavities nucleating in 3D (respectively, 2D plane stress) isotropic elastic bodies the polarization tensor  $\mathbf{A}$  is defined [12]:

$$\mathbf{A} = \frac{3(1-\nu)}{2\mu(7-5\nu)} \left( 5\mathbf{I}_4^{\text{sym}} - \frac{1+5\nu}{2(1+\nu)} \mathbf{I}_2 \otimes \mathbf{I}_2 \right) \quad (3\text{D}), \quad (13)$$

$$\mathbf{A} = \frac{1}{\mu(1+\nu)} \left( 2\mathbf{I}_4^{\text{sym}} - \frac{2\nu^2 - \nu + 1}{2(1+\nu)(1-\nu)} \mathbf{I}_2 \otimes \mathbf{I}_2 \right) \quad (2\text{D plane stress}), \quad (14)$$

while the TS formula, derived e.g. in [3], in the case of transient excitation takes the form:

$$\mathbf{T}(\mathbf{z}) = \{ \hat{\boldsymbol{\sigma}} \star (\mathbf{A} : \boldsymbol{\sigma}) + \rho \hat{\mathbf{v}} \star \mathbf{v} \}(\mathbf{z}), \quad (15)$$

where  $[\boldsymbol{\sigma}, \mathbf{v}]$ ,  $[\hat{\boldsymbol{\sigma}}, \hat{\mathbf{v}}]$ , respectively, are the stress-velocity field pairs,  $\mathbf{v} = \dot{\mathbf{u}}$ , of the free and adjoint forward elastodynamic states, and  $(\star)$  denotes the Riemann convolution in time from  $t = 0$  to  $t = T$ . On the basis of numerical (synthetic) simulations, this task aims to identify the optimal testing configuration under which formula (15) delivers best performance in terms of reconstructing voids in the damaged graphite specimens. For generality, only Block-1 specimen is considered in this task.

For synthetic modeling, SLDV test (detailed in Task 9) performed at  $f_c = 30$  kHz is taken as a basis in the sense that the layout of the scan points and excitation sources are the same as in the actual test, while the experimental SLDV data are replaced by true wavefield simulations on a “defective” mesh shown in Fig. 20. Similar to the SLDV test, the true wavefield is modeled separately for each of the 7 transducer locations shown on the display. In each single-source experiment, the transducer’s impact is reproduced via a Dirichlet boundary condition interpolating the SLDV data obtained from corresponding scan points, while the rest of the specimen is considered traction-free. Using thus obtained synthetic observations data as input, the free and adjoint fields are simulated at durations ranging from  $T = \tau$  to  $T = 6\tau$ . Following [26], adjoint field virtual excitation is also time-windowed with a smoothing period  $\Delta T = 0.25/f_c = 8 \mu\text{s}$  to avoid nonzero initial conditions. Using (15), single-source TS distributions are calculated and subsequently summed up yielding the final multi-source reconstruction maps.

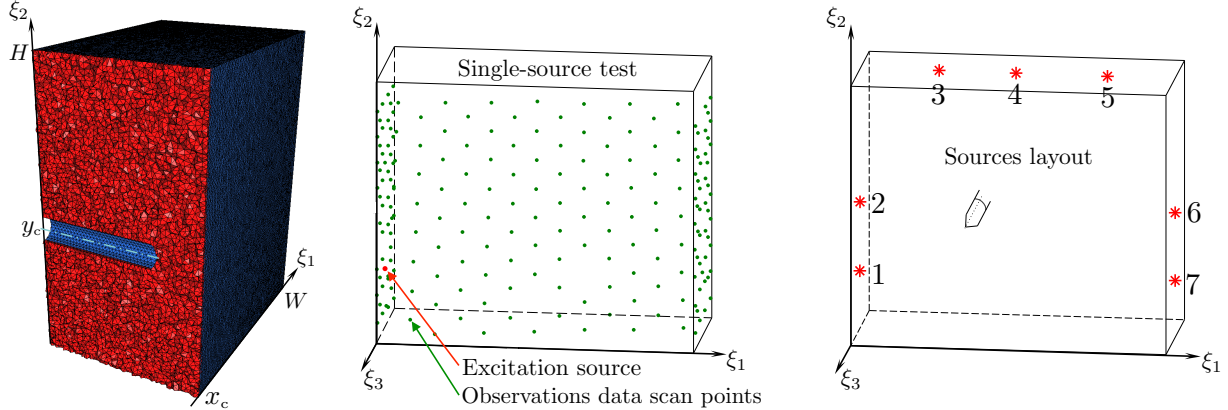


Figure 20: Synthetic observations data reconstruction via “defective” FE mesh for Block-1 specimen.

To assess the quality of the TS-based reconstruction under various testing conditions, a parametric study was conducted by varying: i) source aperture  $S \subseteq \{1, 2, 3, 4, 5, 6, 7\}$  signifying the collection of excitation sources in Fig. 20, and ii) duration of the observation period  $T \in \{\tau, 2\tau, \dots, 6\tau\}$ . Since computed TS fields exhibit pronounced negative values in the immediate vicinity of  $\partial\Omega$  [26] inherently leading to erroneous defect reconstruction, the spatial distributions of the TS maps were truncated at distances  $d \leq d_{\text{tr}} = 25$  mm from the margins of the block.

Fig. 21 shows individual contributions of the first six sources to the reconstruction of the cavity defect obtained at  $T = 6\tau$ , where the source position is indicated schematically via star-shaped markers. For better visualization, the 3D TS maps are given in terms of several plane projections featuring two planes  $\xi_1 = x_c$  and  $\xi_2 = y_c$  intersecting along the axis of the void, and 4 planes normal to the axis of the void located at  $\xi_3 = -0.4D$ ,  $\xi_3 = -0.5D$ ,  $\xi_3 = -0.6D$ , and  $\xi_3 = -0.7D$ . To focus on the negative values of the TS, positive values are not shown on the maps, while each plane projection is conveniently normalized to the minimum value of  $-1$ . As seen from the display, single source maps are contaminated to various extent with spurious



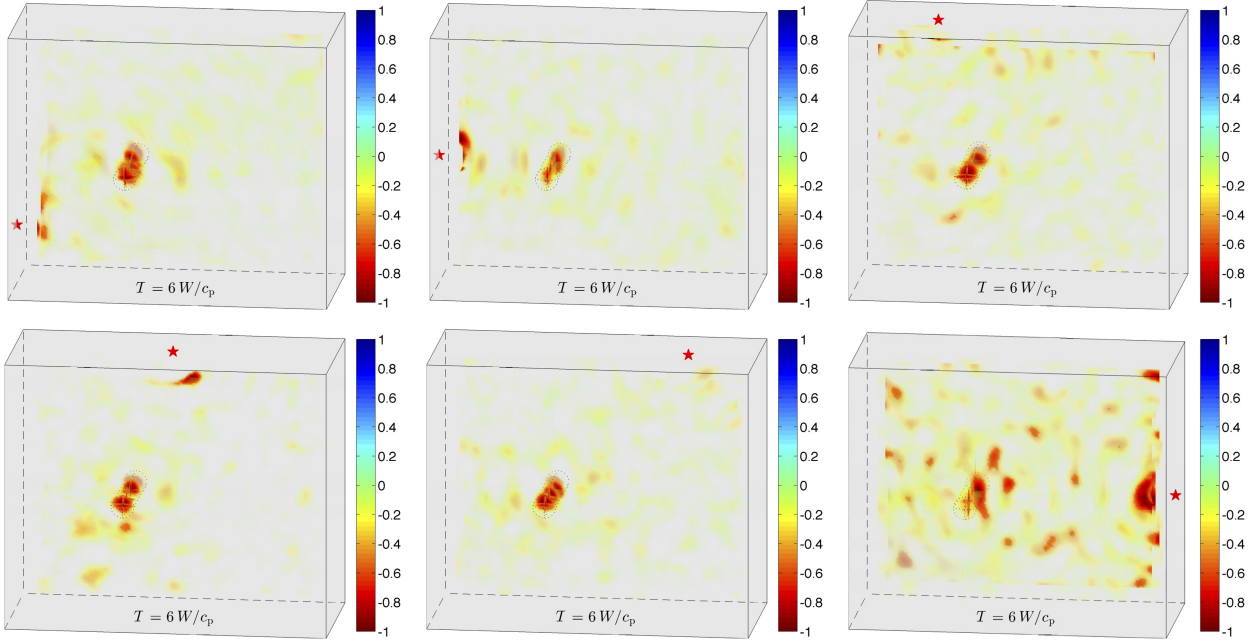


Figure 21: Contribution of individual sources to synthetic reconstruction of the cavity defect in Block-1 specimen obtained at  $f_c = 30$  kHz,  $T = 6W/c_p$ .

minima not affiliated with the void deteriorating the reconstruction. In general, summing up maps from various sources helps level out such spurious minima while emphasizing the true minimum circumscribing the defect, see Fig. 23.

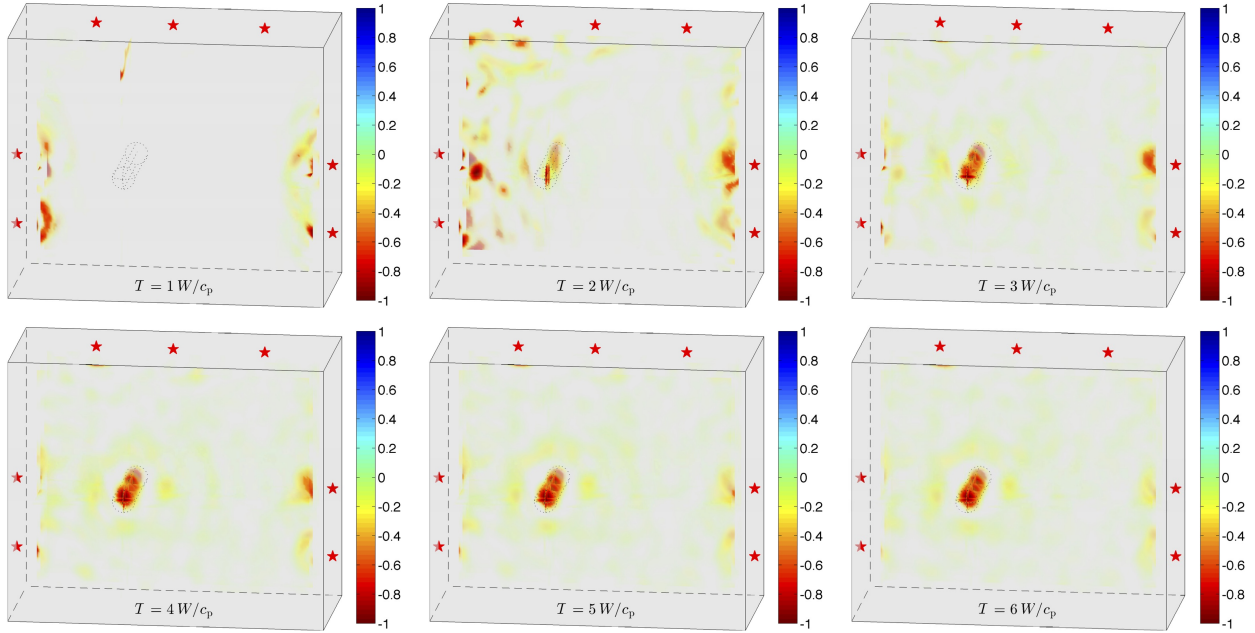


Figure 22: The effect of duration  $T$  on synthetic reconstruction of the cavity defect in Block-1 specimen obtained at full source aperture  $S = \{1, 2, 3, 4, 5, 6, 7\}$  and  $f_c = 30$  kHz.

The effect of duration of the observation period  $T$  is shown in Fig. 22, featuring TS maps obtained at full source aperture and varying  $T$  in terms of characteristic time  $\tau = W/c_p$ ,  $W = 364$  mm. As pointed out in [26], there are two competing phenomena that might affect the quality of TS reconstruction when changing  $T$ . Firstly, there is a time scale  $T_b = 5/f_c = 1.2\tau$  affiliated with the duration of the excitation burst (see Fig. 26) negatively affecting TS map when  $T \leq 2T_b \simeq 2.4\tau$ . On the other hand, there is the spurious wave dispersion in the numerical FE solution, whose adverse effect accumulates with the distance traveled, i.e. with

increasing duration  $T$ . In the case of synthetic testing, as opposed to the actual experiment in Task 9, the latter effect is much less pronounced since numerical dispersion is effectively canceled by the fact that any numerical infidelity introduced to the propagation of the free and adjoint wavefields will be present at the same level in the true wavefield provided similar spatiotemporal discretizations of the true/reference domains. Also known as *inverse crime*, this effect is specific to any inverse problem exposed to synthetic observations data [9].

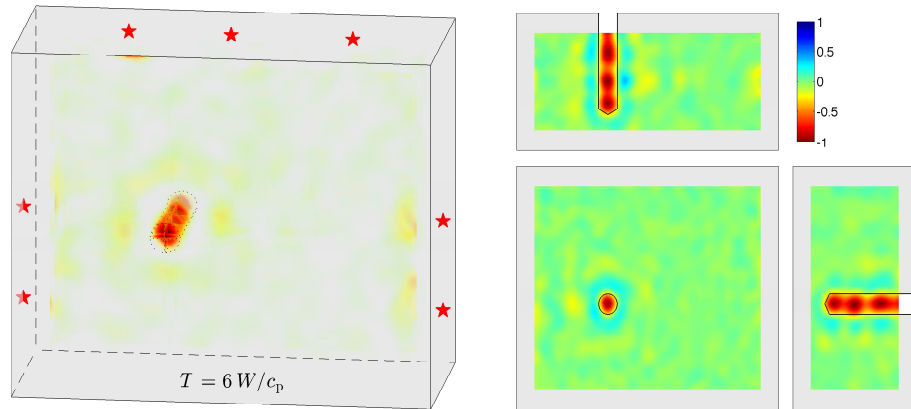


Figure 23: Full aperture,  $T = 6\tau$ ,  $f_c = 30$  kHz synthetic TS map obtained in Block-1 specimen. Planar views on the right panel feature three mutually orthogonal projections:  $\xi_1 = x_c$ ,  $\xi_2 = y_c$ ,  $\xi_3 = -0.5D$ ,  $(x_c, y_c)$  being the center of the cavity in  $\xi_1$ - $\xi_2$  plane.

## Task 6: Acquisition and implementation of the SLDV testing system

Boundary data acquisition is effected via a scanning LDV system PSV-400-3D by Polytec, Inc. By deploying the principles of optical interferometry and three independent scanning heads targeting a material point from different angles as shown in Fig. 24, the system is capable of capturing the normal and in-plane velocity components of the surface motion over a prescribed grid of points with the spatial resolution better than 0.1 mm. The data acquisition is performed using a built-in velocity decoder VD-03 with the sensitivity and sampling frequency  $F_s$  set respectively at 10 mm/s-V and 2.56 MHz. At these settings, the velocity resolution of the LDV system is approximately 300  $\mu\text{m/s}$  for frequencies below 100 kHz, and the amplitude error is  $\pm 0.1$  dB at 1 kHz. To minimize the effect of random noise in the system (both optical and mechanical), signal stacking is implemented over an ensemble of 50-100 realizations at each scan point. To avoid signal dropouts due to inherent surface roughness, signal enhancement and speckle tracking are enabled during data acquisition. All internal filters, both analogue and digital, were disabled to exclude phase-related errors in the observed surface motion. The scan heads are positioned at stand-off distance of roughly 60-90 cm from the center of the object such that all scan points can be reached by each unit with the deflection angle (i.e. the angle between the laser beam and the axis of the scan head) less than 20 degrees. 3D alignment is performed conveniently with the manufacturer-provided rangefinder device (geometry scan unit) that measures distances with the accuracy about 2 mm. Given scan points lying on the plane (e.g., edge of a block), a sufficient accuracy of the 3D alignment is reached with 4 reference points located in the farthest corners of the scan points area and at least one more reference point set along the normal to the plane, about 15-30 cm toward the scan heads.

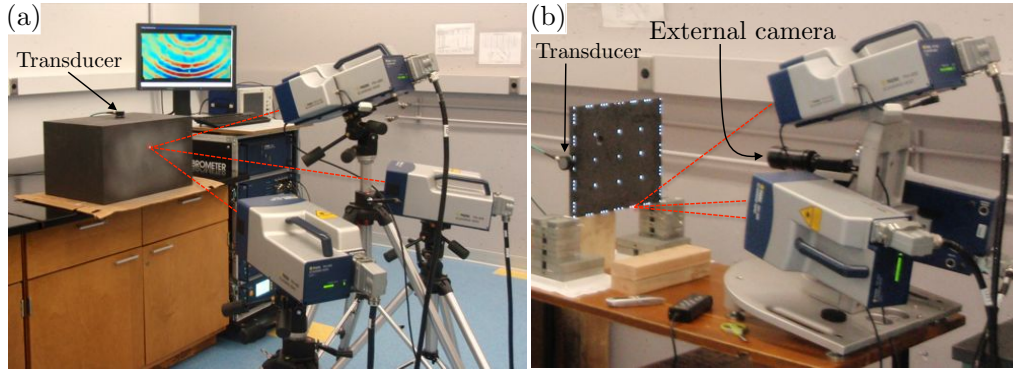


Figure 24: LDV setups for testing graphite with heads positioned on: a) floor tripods, b) table tripod.

### Dynamic excitation

Dynamic excitation of the graphite unit is provided by either a 32 mm-diameter, 0.5 MHz (Olympus V101), or a 16 mm-diameter, 1.0 MHz (Olympus V103) contact piezoceramic longitudinal wave transducer attached to the graphite via cyanoacrylate glue. The 0.5 MHz transducer is used for specimens Plate-1 and Plate-2 and is attached to a plate's edge such that the axis of the transducer is approximately aligned with the mid-plane of the plate (display (b)) thus minimizing the out-of-plane motion. The 1.0 MHz transducer is used for testing Block-1 specimen and is attached to the graphite via a transfer rod with a cross-section reduction from 16 mm to 6 mm, see display (a). The rod is intended to enable LDV accurately measure the excitation in all three directions, see Task 8. The transducer is excited by a 5-cycle wavelets shown in Fig. 26 whose dominant frequency  $f_c$  ranged in the experiment from 10 kHz to 40 kHz. To generate the wave motion of sufficient amplitude, the output from the signal generator is intensified by high-voltage, 2 kW radio-frequency amplifier with the flat gain spectrum at 9-250 kHz.

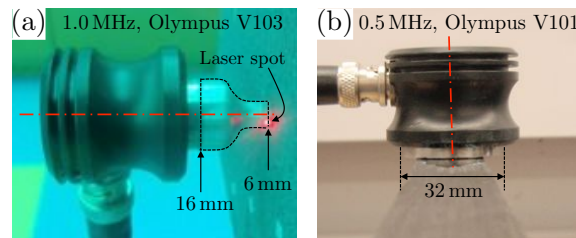


Figure 25: Piezoceramic transducers utilized for the excitation of: a) Plate-1, Plate-2, b) Block-1 specimens.

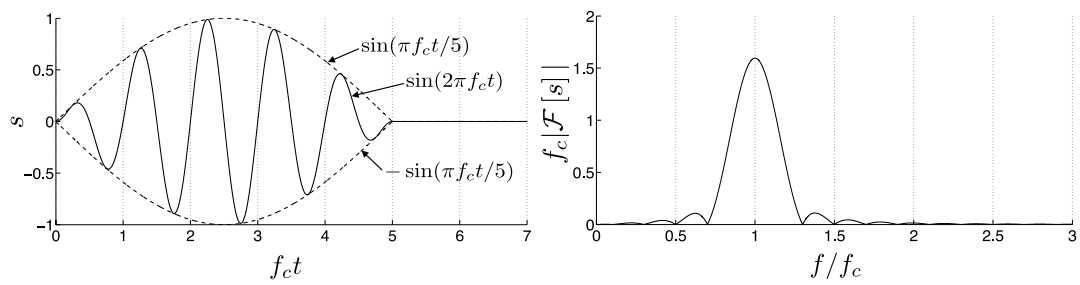


Figure 26: Excitation signal in the time and frequency domains.



## Task 7: Element testing of graphite specimens

Aimed at verifying the isotropic constitutive behavior of nuclear graphite and obtaining its elastic moduli, several ultrasonic bench tests were performed on several intact graphite specimens. For Block-1 specimen, the velocities of the compressional P- and shear S- waves were measured in a series of transmission tests with transducers located on the opposite sides of the block yielding propagation in various directions. The discrepancy between the registered velocities was less than 2% for P-wave and less than 1% for S-wave, which within the accuracy of the measuring device renders isotropic behavior of the graphite. As for specifying the elastic properties of the graphite, bench measurements were conducted at 1 MHz transmission on a selection of auxiliary smaller graphite specimens not involved in the SLDV testing. The results, including the measured quantities: mass density  $\rho$ , P-wave velocity  $c_p$ , S-wave velocity  $c_s$ , and the derived elastic moduli: Poisson's ratio  $\nu$ , Young's modulus  $E$ , and shear modulus  $\mu$ , are presented in Table 1.

Sample	$\rho$ [kg/m <sup>3</sup> ]	$c_s$ [m/s]	$c_p$ [m/s]	$\nu$	$E$ [GPa]	$\mu$ [GPa]
1	1849	1578	2693	0.24	11.41	4.60
2	1832	1443	2605	0.28	9.76	3.82
3	1835	1445	2648	0.29	9.87	3.83
4	1845	1458	2676	0.29	10.11	3.92
5	1847	1597	2680	0.22	11.54	4.71
6	1835	1451	2610	0.28	9.86	3.86
7	1849	1448	2667	0.29	10.01	3.88
8	1849	1444	2614	0.28	9.87	3.86
9	1847	1462	2680	0.29	10.17	3.95

Table 1: Ultrasonic bench measurements of a selection of graphite specimens.

As seen from the table, most of the specimens yield similar elastic moduli except for samples 1 and 5 whose Young's moduli are about 15% higher than the average of the rest. Such discrepancy could be induced due to manufacturing process. With the TS-based reconstruction, if the elastic properties of the reference medium are not determined exactly, i.e. differ from the parameters of the tested material, the model wavefields will develop a lag/advance with respect to propagation of the true ultrasound waves on top of any dispersion existing in the numerical model itself. Thereby induced propagation error will affect the TS map in a linear fashion since TS is a linear function of the dataset (15). To quantify the propagation error, one may use the dimensionless ratio  $\Delta T/T_0$ , where  $\Delta T$  is a phase shift of the model and  $T_0$  is a period of the wave. Since  $\Delta T = |L/c_p - L/c_p^{\text{mod}}|$ , where  $c_p^{\text{mod}} \neq c_p$  is a model velocity,  $L$  - distance traveled by the wave, and  $T_0 = 1/f$  - period of the wave,  $f$  - frequency of the wave:

$$\frac{\Delta T}{T_0} = f \frac{L}{c_p^{\text{mod}}} \frac{|c_p^{\text{mod}} - c_p|}{c_p} = fT \frac{|c_p^{\text{mod}} - c_p|}{c_p}, \quad (16)$$

where  $T = L/c_p^{\text{mod}}$  is the duration of propagation. Therefore, the propagation error is proportional both to the frequency of the illuminating wave, and the duration of propagation. Note that if reconstruction is performed at high frequencies and longer durations, even small relative velocity error can produce significant propagation error and lead to an erroneous TS map. To this end, additional ultrasonic tests were performed on the genuine graphite specimens, results presented in Table 2. All three specimens were originally made out of a single block and thus have the same properties further utilized in 2D and 3D FE models. One can notice that the measured elastic moduli are similar to those of samples 1 and 5 in the bench tests. On the other hand, the similar test conducted on another available graphite block specimen, not used for SLDV testing, showed elastic properties closer to the rest of the bench test specimens.

Specimen	$\rho$ [kg/m <sup>3</sup> ]	$c_s$ [m/s]	$c_p$ [m/s]	$\nu$	$E$ [GPa]	$\mu$ [GPa]
Plate 1, Plate 2, Block 2	1842	1573	2725	0.25	11.4	4.56

Table 2: Ultrasonic measurements of the specimens from Task 1.

## Task 8: SLDV testing of damaged VHTR core components

### SLDV data acquisition

Figs. 27 and 28 show testing setups for SLDV data acquisition from, respectively, Plate-1/Plate-2 and Block-1 specimens. During testing, special supports/props were employed to elevate the specimens above the ground level minimizing non-traction-free surfaces: plate specimens 1 and 2 were secured in place (by own weight) using contact patches at the bottom corners, while Block-1 specimen was set onto three legs located in the vertices of an equilateral triangle (see display (a) in Fig. 28). Excitation was provided by the piezo transducers (see Task 6) and the induced motion was monitored at a set of scan points on the surface of the graphite both in terms of observations and excitation data.

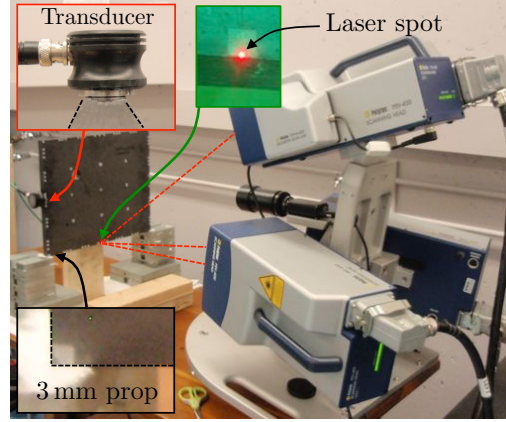


Figure 27: 2D SLDV data acquisition: Plate-1 and Plate-2 specimens.

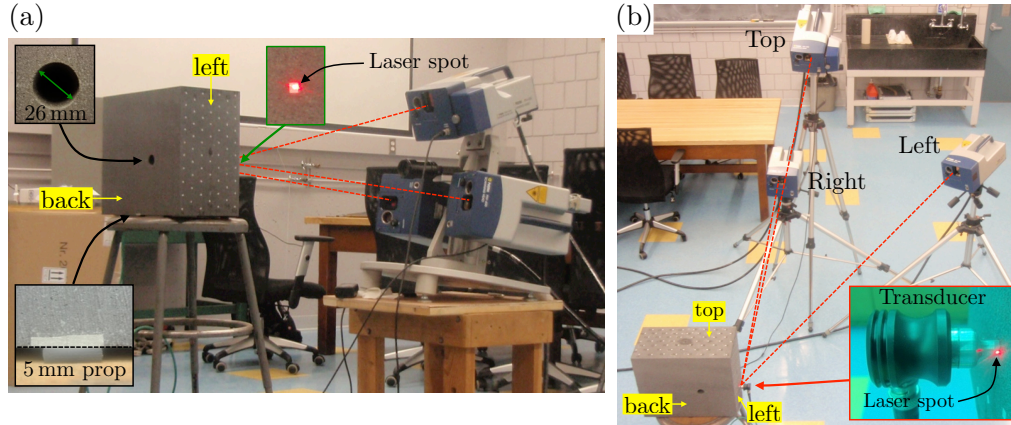


Figure 28: 3D SLDV data acquisition: Block-1 specimen.

For the purpose of measuring excitation data, additional scan points were set in the vicinity of the transducer contact patch to collect the data further utilized in numerical simulations as input Dirichlet data. In this vein, testing of Block-1 specimen (Fig. 28) required two different SLDV setups: for observations data acquisition the scanning heads were set on a table tripod as shown in display (a), while the floor tripods were employed for excitation data acquisition, display (b). The first setup allows quick relocation of the scan heads for measurements on different sides of the block, while the second setup is only necessary for locating laser beams on the transfer rod attached to the transducer. Note that the transfer rod enables to shoot the lasers at a greater angle with respect to each other facilitating measurement with sufficient sensitivity in both lateral and axial directions of the transducer's motion (specifically, in display (b) the left laser can be set further apart from the other two). Note also that the reduced output cross-section of the transfer rod (see also Fig. 25) helps concentrate the impact of the transducer on a smaller patch thus enabling SLDV to measure excitation more precisely. As for testing the plate specimens, both observations and Dirichlet data were collected in a single experiment thanks to simplified 2D configuration of the units, see Fig. 27. To enhance backscattering from graphite surface retroreflective tape was employed in locations of the scan points (visible in the figures),

however, as shown in quarterly report 8, sufficient signal-to-noise ratio can be achieved on bare graphite surface provided more elaborate laser focusing.

Obtained SLDV velocity signals were processed in MATLAB, namely band-pass filtered in the range  $[0.5f_c, 1.5f_c]$ , numerically integrated, and filtered again rendering noise free displacement data. An example of thereby processed data obtained from the Block-1 specimen at excitation frequency  $f_c = 30$  kHz, is shown in Fig. 29. An estimate of the relative error of the measured signals can be judged from the characteristics of the utilized velocity decoder VD-03. In absence of mechanical/optical noises, the decoder yields velocity uncertainty of  $\Delta v = 300 \mu\text{m/s}$ , the corresponding displacement uncertainty is  $\Delta u = \Delta v / F_s \approx 0.1 \text{ nm}$ . After averaging over  $N$  independent realizations, the uncertainty is reduced by a factor of  $1/N$ , rendering the relative error for the signals at 1 nm amplitude (e.g., observations in Fig. 29) stacked at 50 realizations, on the order of 0.2 %.

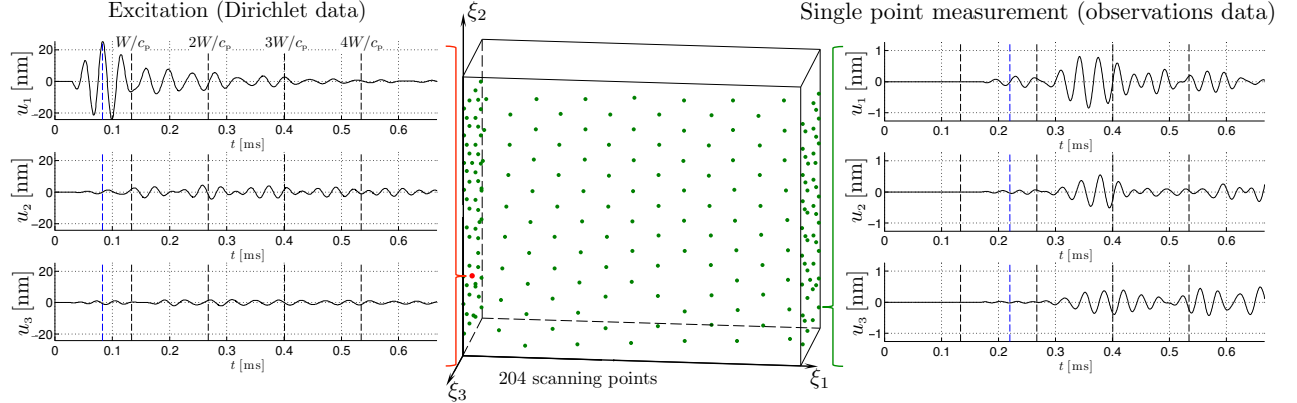


Figure 29: 3D LDV data: Dirichlet excitation and observations

## Comparison between the experimental SLDV and numerical FE model data

In order to assess the accuracy of the forward elastodynamic simulations the “true” field FE models were utilized to simulate wave propagation in the damaged specimens Plate-1 and Block-1. In the simulations, the SLDV-acquired excitation data were rendered as input Dirichlet data. The accuracy of the numerics was then judged by comparing the FE-generated displacement time histories to the processed (filtered and integrated) SLDV signals at several scan points. Shown in Fig. 30 and Fig. 31 are the displacement signals obtained with  $f_c = 10$  kHz excitation at three different scan points for, respectively, Plate-1 and Block-1 specimens. As seen from the displays, chosen numerical platform allows to reconstruct the wavefields reasonably well even after the P-wave travels 4–5 lengths of the specimen, i.e. up to durations  $T = 5\tau$ . Also, no significant change in the wavefield records was registered, both in terms of LDV and FEM simulated data, when the location of the aforementioned legs was altered which justifies the use of a simplified boundary conditions model when the full surface of the specimen is assumed traction-free except for the excitation patch/section where Dirichlet data are to be specified.

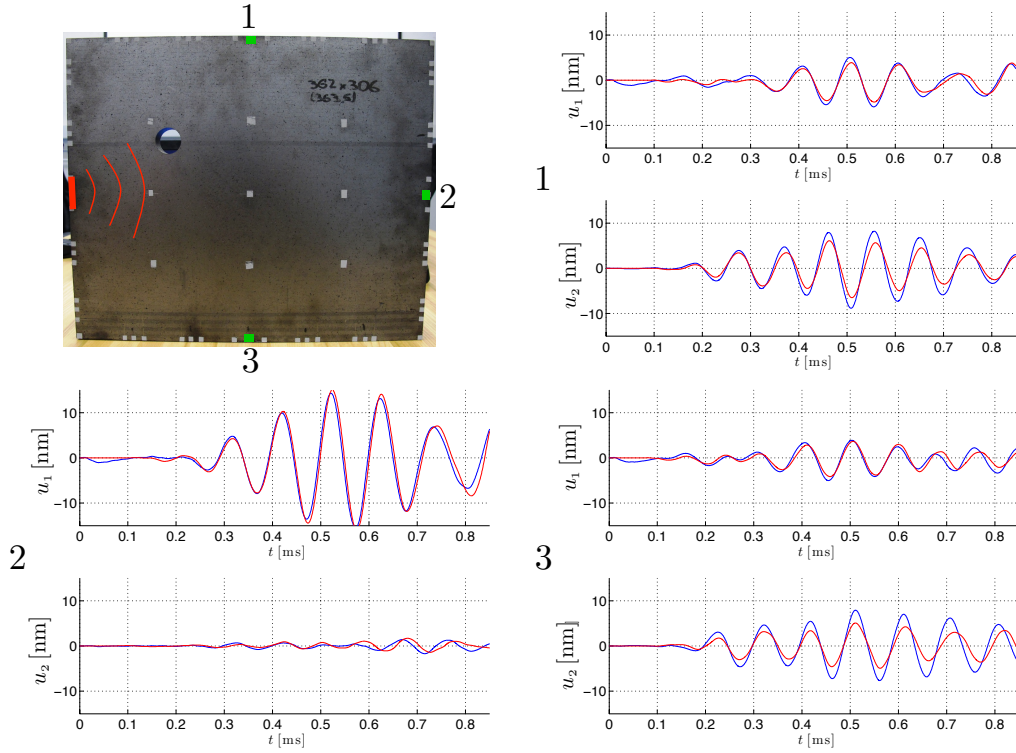


Figure 30: 2D FE displacement data vs. SLDV experimental data in Plate-1 specimen.

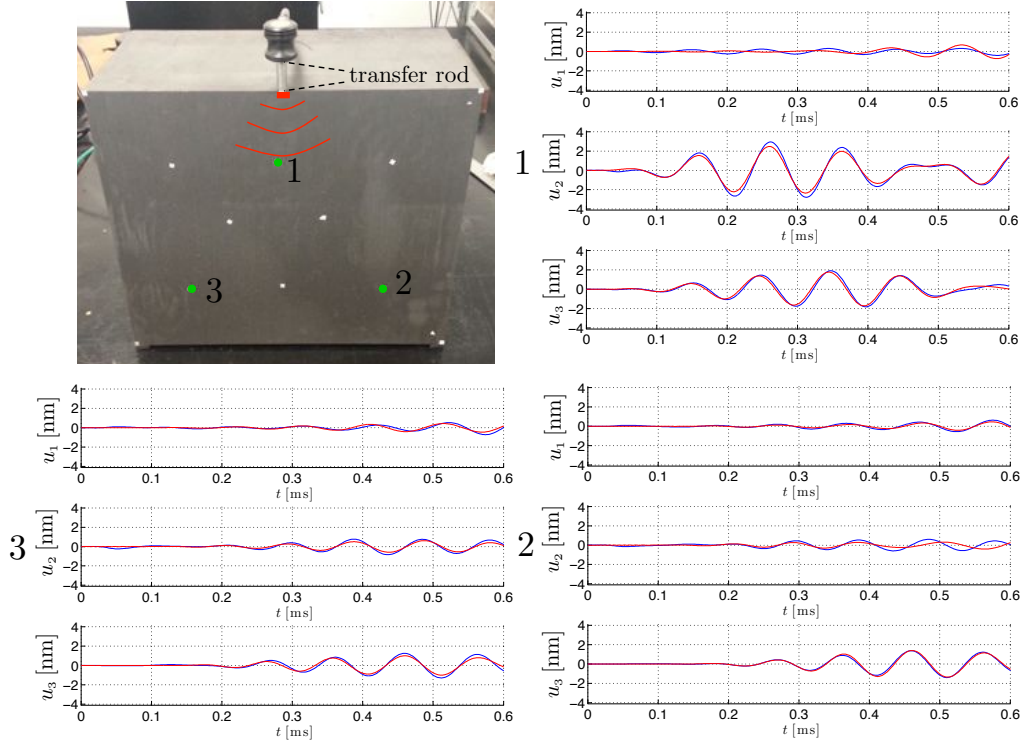


Figure 31: 3D FE displacement data vs. SLDV experimental data in Block-1 specimen.

## Discontinuous Galerkin upgrade of the finite element (FE) model

Further studies on FE modeling showed a great sensitivity of the simulated data to the spatiotemporal discretization of the numerical method especially at higher frequencies and longer simulation durations since the chosen numerical scheme though computationally cheap and easy to implement, is not well suited for wave propagation problems [18, 22]. To mitigate numerical infidelity several approaches are proposed in the litera-

ture as how to enrich the FE formulation, see e.g. [15, 16]. On the other hand, a considerable attention has been given to the development of Discontinuous Galerkin (DG) FE formulations [8]. A promising numerical scheme in this case is so-called Arbitrary high-order DERivative Discontinuous Galerkin method (ADER-DG) based on the hyperbolic formulation of the system of elastodynamics [19]. As an illustration of the capabilities of this technique, a fundamental elastodynamic problem in an infinite graphite plate is simulated using polynomials of 8th degree on a very coarse mesh (about 0.5 elements per wavelength) and compared to the analytical wavefield function, see Fig. 32. Note that the numerical and analytical solutions almost match as far as 7 wavelengths from the origin, i.e. almost no numerical dispersion is introduced to the simulated wavefield.

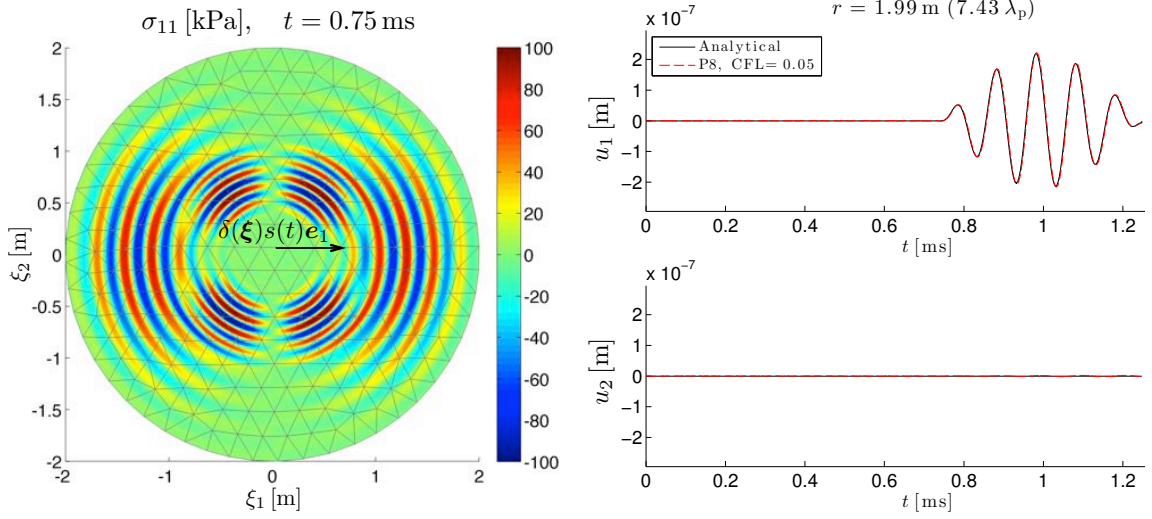


Figure 32: Fundamental elastodynamic solution simulated with ADER-DG.

## Task 9: TS imaging and characterization of damage from SLDV measurements

### 2D reconstruction in Plate-1 and Plate-2 specimens

As shown in Task 5 and previous numerical studies the performance of TS-based defect reconstruction is strongly affected by the apertures of both source and observation grids. In particular, each of the two grids should maximize the solid angle around the (expected) damaged region to make the best use of a fixed number of experimental measurements. In this vein, the testing configuration adopted for the plate experiments is shown in Fig. 33, consisting of four excitation patches (transducer locations), illuminating the hole/slit from four directions as shown in display (a), while the induced elastodynamic wavefield is monitored over SLDV scan points located in the immediate vicinity of the plate's edges whose germane layout is shown in display (b). In the experiment, the source transducer is first placed at location 1 and motion sensing is then performed at the corresponding set of scan points (both observation and excitation) and the data thus obtained are used to compute the free and adjoint elastodynamic states whose bilinear form (15) gives the affiliated TS distribution. The source transducer is then moved to the second location, for which the testing and computational procedure are performed anew. In what follows, the superposition of these individual TS distributions is used as a reconstruction map.

To facilitate discussion on the influence of the duration and the excitation frequency on the quality of the experimental TS reconstruction, the maps obtained at different  $f_c$  and  $T$  are organized in tables shown in Fig. 34 (Plate-1) and Fig. 35 (Plate-2). In the latter, the maps are only plot in the neighborhood of the slit defect for better visualization. As seen from the first display, the hole defect is clearly detected in terms of well-defined minimum on the  $f_c = 10$  kHz and 20 kHz maps while at higher center frequencies the corresponding minimum is much less pronounced which is the consequence of numerical error introduced to simulations due to presence of higher frequencies in the excitation spectrum (see Fig. 26). The latter not only have adverse effect on the accuracy of the numerical scheme but might also be improperly approximated by the plane stress assumption (see Task 4). Note also the effect of duration: at lower frequencies the maps improve as  $T$  increases in accordance to the numerical studies in Task 5, however at higher frequencies increasing duration  $T$  has a negative effect on the reconstruction maps as more error is accumulated in the numerical simulations. In case of reconstructing the slit defect in Plate-2 specimen, Fig. 35, similar effects can be observed, however lower frequency maps  $f_c = 10$  kHz and 20 kHz provide poor evidence of the damage due to insufficient interaction/scattering of the long wavelength illumination with the crack also obscured by the hole defect. On the other hand,  $f_c = 30$  kHz map renders at  $T = 6\tau$  much more accurate reconstruction of the obstacle thanks to denser mesh (see Fig. 17) and, therefore, reduced numerical error. In addition, the negative effect of duration  $T$  is somewhat minimized in this way, see also  $f_c = 40$  kHz maps.

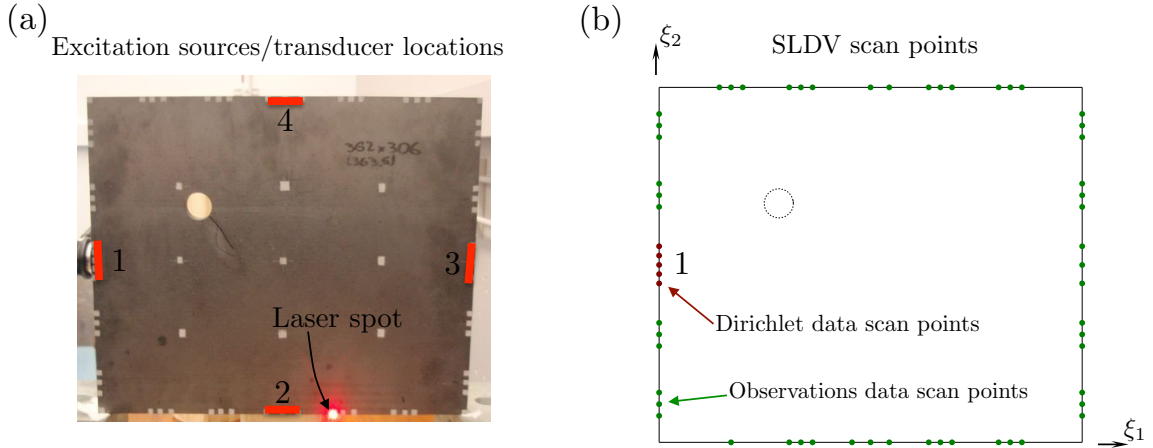


Figure 33: Scan points layout and transducer locations for testing Plate-1 and Plate-2 specimens.



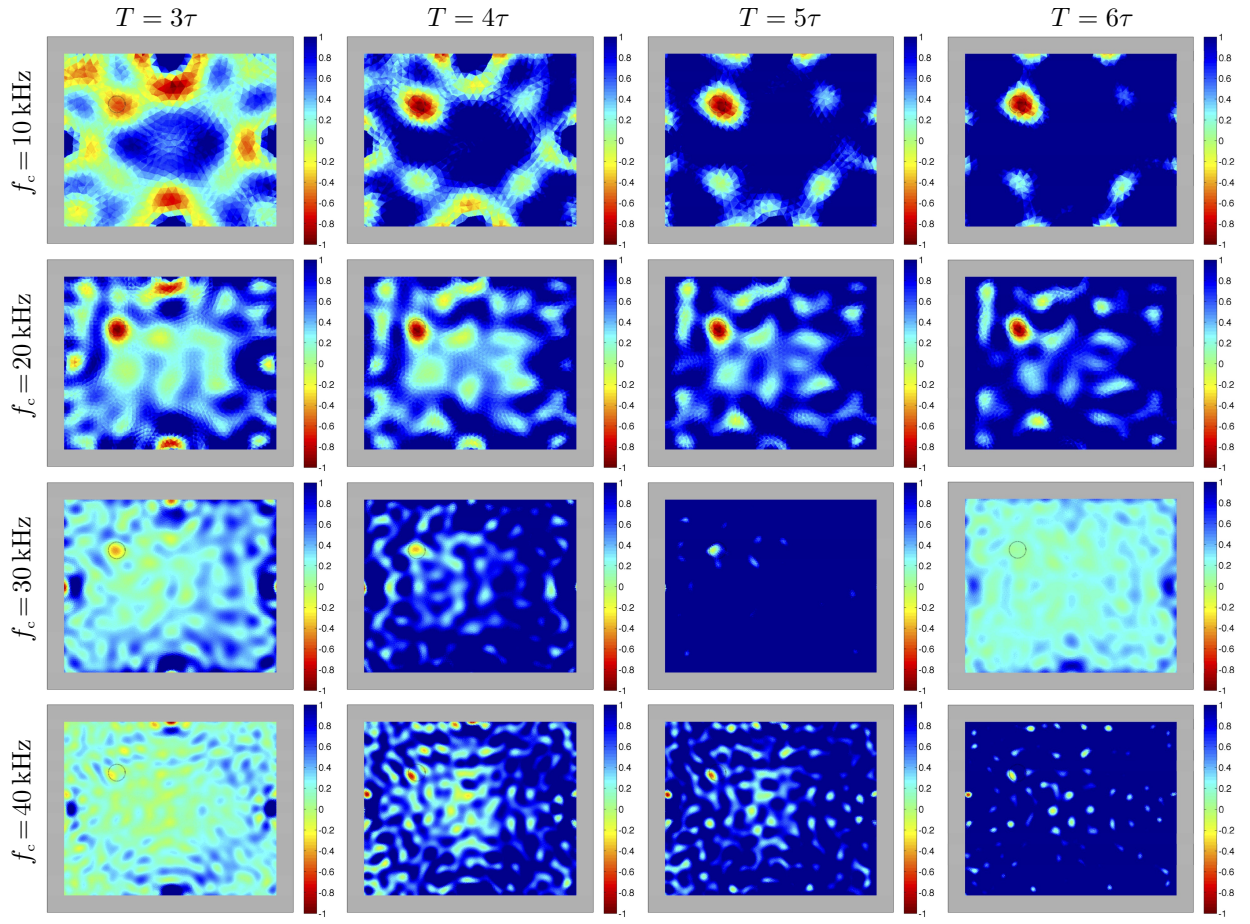


Figure 34: 2D TS maps obtained in Plate-1 specimen at different excitation frequencies  $f_c$  and durations  $T$ .

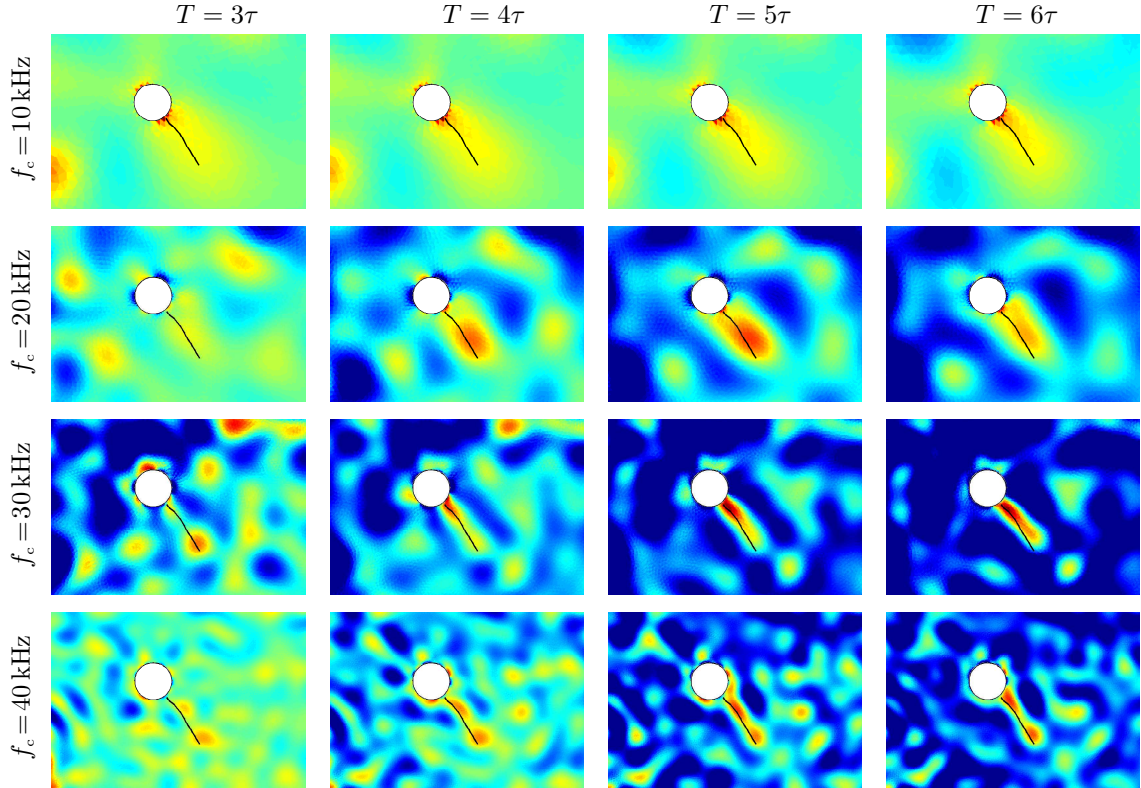


Figure 35: 2D TS maps obtained in Plate-2 specimen at different excitation frequencies  $f_c$  and durations  $T$ .



### 3D reconstruction in Block-1 specimen

Fig. 36 presents the configuration of the scan points and transducer locations for testing Block-1 specimen. Here, the transducer (Fig. 25a) was consequentially attached to the left, top, and right edges of the block as shown in display (a), while the wavefield motion was monitored on a set of scan points distributed over the left, front, and right edges of the block, see display (b). The resulting reconstruction maps (obtained upon summing the single-source TS distributions) are presented in Fig. 37 in terms of three planar views:  $\xi_1 = x_c$ ,  $\xi_2 = y_c$ ,  $\xi_3 = -0.5D$  with  $(x_c, y_c)$  denoting the center of the cavity in  $\xi_1$ - $\xi_2$  plane, and in Fig. 38 in terms of three-dimensional assembly of these projections (positive values neglected) with normal planes added at  $\xi_3 = -0.4D$ ,  $\xi_3 = -0.6D$ , and  $\xi_3 = -0.7D$ . Note the pronounced deterioration of the  $f_c = 30$  kHz map as duration  $T$  increases above  $T = 5\tau$  due to infidelity of the numerical model which in 3D case becomes more sensitive to spatiotemporal discretization as the number of elements is dramatically increased, see Fig. 17.

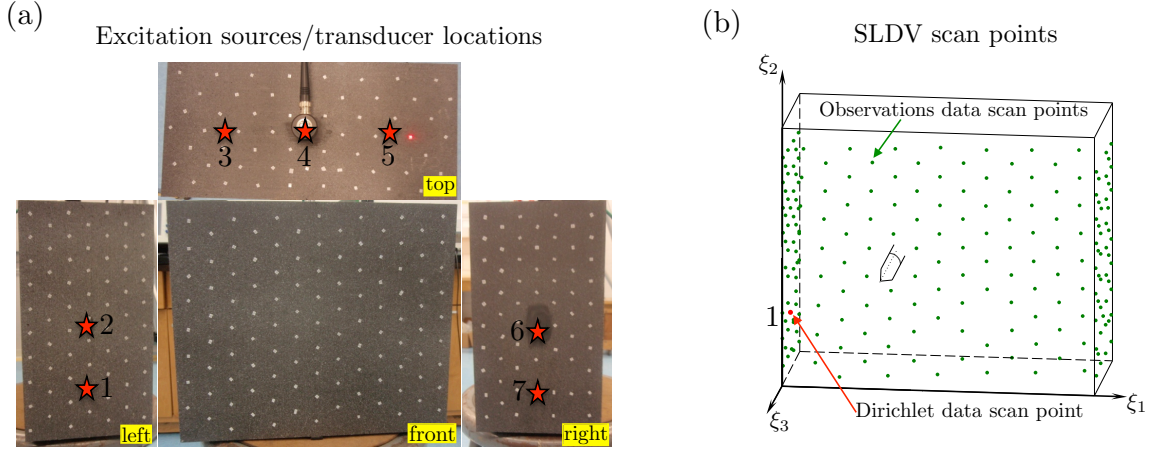


Figure 36: SLDV setup for testing Block-1 specimen.

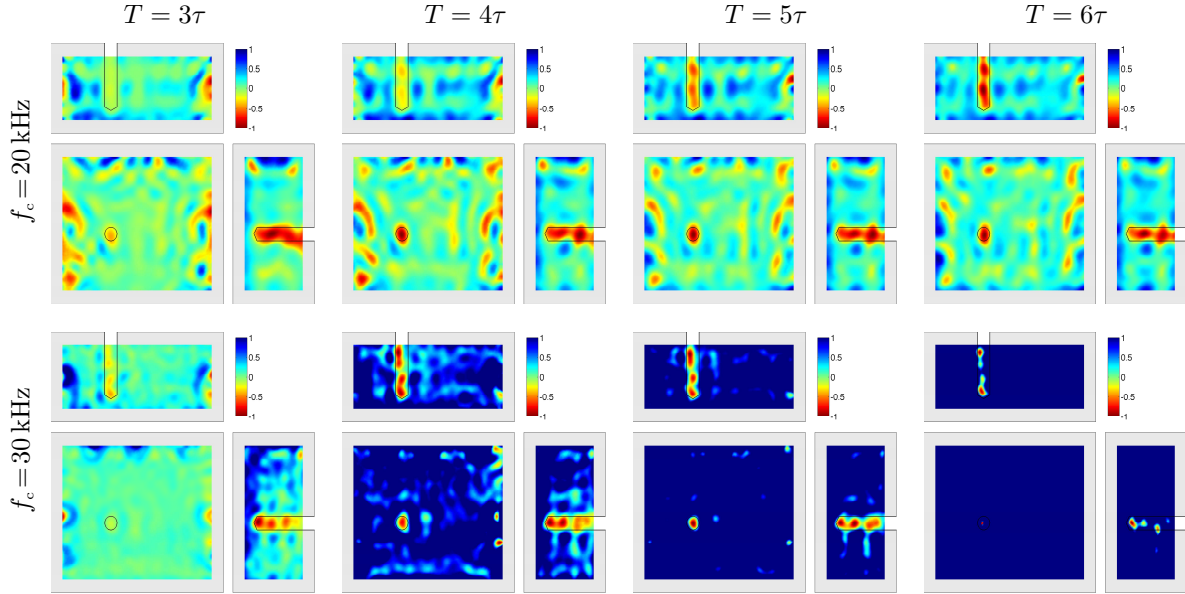


Figure 37: Planar views of the reconstruction maps obtained in Block-1 specimen at different excitation frequencies  $f_c$  and durations  $T$ .

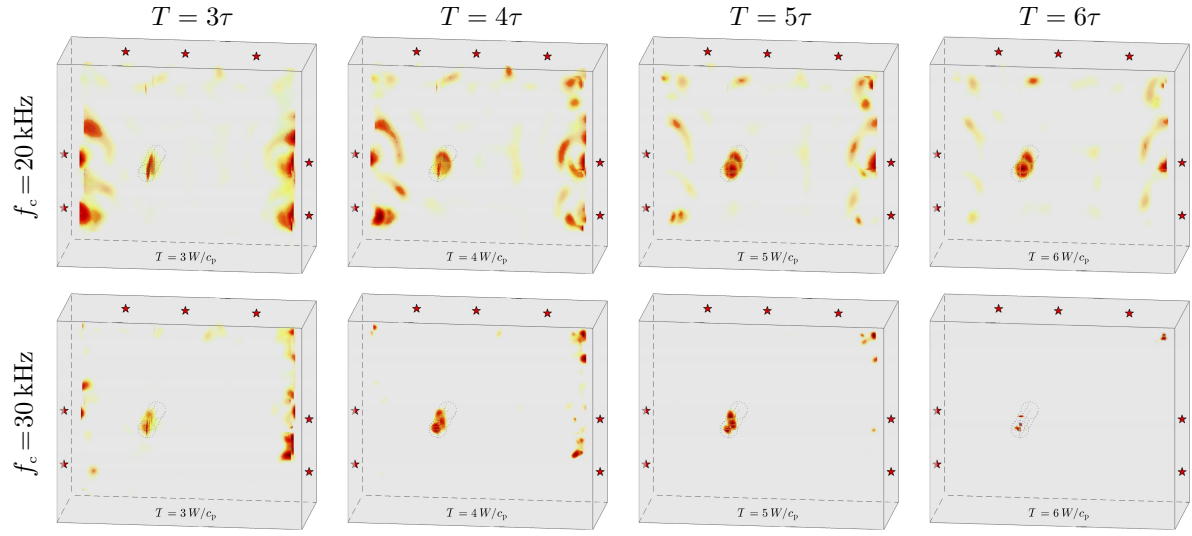


Figure 38: Reconstruction maps obtained in Block-1 specimen at different excitation frequencies  $f_c$  and durations  $T$ .

## Task 10: Verification: comparison with CT scans

Since the Computed Tomography (CT) imaging in Task 2 of a nuclear graphite specimen with *diffuse damage* (induced by uniaxial compression) did not yield any signs thereof, it was not fruitful to pursue the TS-SLDV testing of that block. On the other hand, the damage in blocks that have been used for the TS-SLDV imaging is of *discrete type* (as created by machining) – which by definition does not require verification by CT scanning.

*On the detection of diffuse material damage.* It is, however, hypothesized that the diffuse damage in quasi-brittle materials, manifesting itself in the form of *micro-cracks*, could possibly be sensed by the *macroscopic* (centimeter-long) elastic waves such as those featured in this project. To explore this possibility, a preliminary one-dimensional (experimental and analytical) study was performed to investigate the hypothesis. In particular, it is shown [10] that the macroscopic waves may sense the presence of microscopic damage via the *dispersion* of waves propagated through a diffusely-damaged material. This is shown in Fig. 39 which shows the experimental setup, and Fig. 40 which illustrates the microstructure-induced dispersion (i.e. the dependence of the wave speed on frequency) of elastic waves in the damaged section of an aluminum rod.

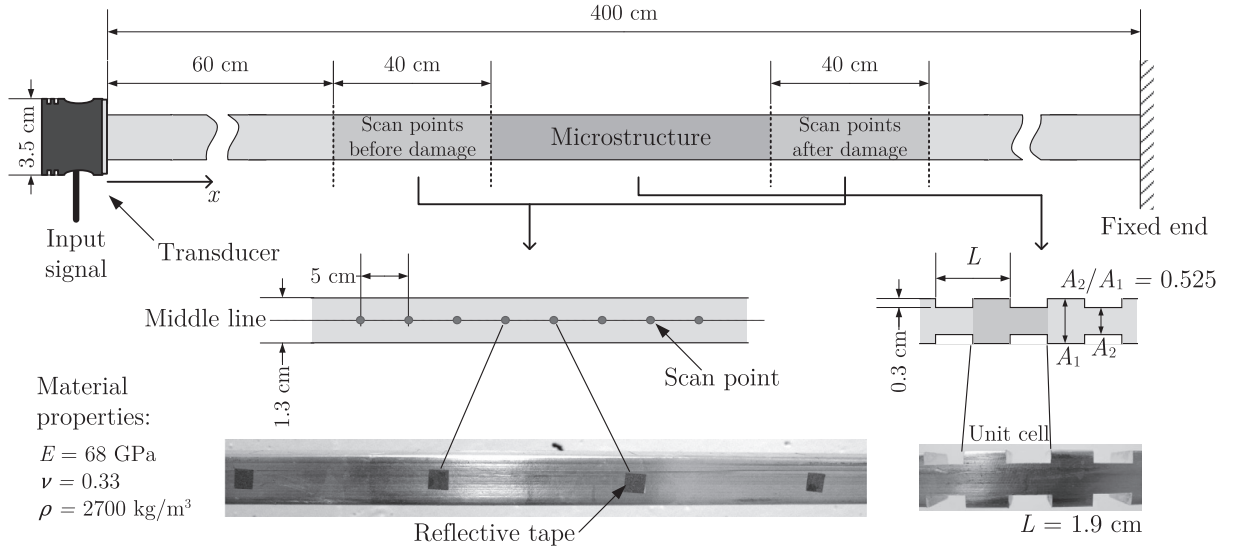


Figure 39: Schematics of the experimental setup.

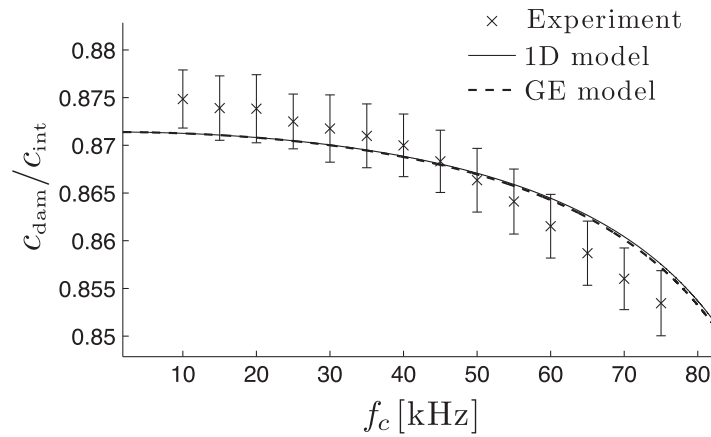


Figure 40: Variation of the phase velocity of longitudinal waves in a damaged section of the aluminum rod.

## Task 11: Comparison with existing NDE methodologies

For demonstration purposes, a series of A-scans were carried out in Block-1 specimen using an ultrasonic test system James V-meter Mark II consisting of a pulse generator/oscilloscope, and two 54 kHz P-wave piezoceramic transducers, see Fig. 41. The system was set to measure the direct transmission time of an ultrasonic P-wave propagating along the largest dimension of the block with the transducer pairs located at different heights along the left and right edges of the block, see display (b). As expected, the measured time-of-flight experienced a jump when the transducers were set on the line intersecting the support of the cavity, see display (c). In this way, only an approximate location in terms of height at which the defect is present can be determined from the acquired data, while no information can be derived in terms of the size or the shape of the defect. Given more source-receiver pairs one may, of course, obtain more information; however in the limited aperture case that is relevant to the periodic inspection of in-service VHTR components, it is impossible to reconstruct the defect from just the time-of-flight measurements – which is the key advantage of the TS-based technique. Moreover, the accuracy of ultrasonic measurements is limited by the wavelength, which is inversely proportional to the frequency of the transducer, so very high frequencies are required to obtain good resolution reconstruction. In the elements of nuclear graphite however, higher frequencies might experience reflections from the internal pores and thus affect the quality of the transmission test. In contrast, the TS-based reconstruction operates with the so-called sub-wavelength resolution, i.e. the TS maps are capable of imaging defects that are smaller the illuminating wavelength.

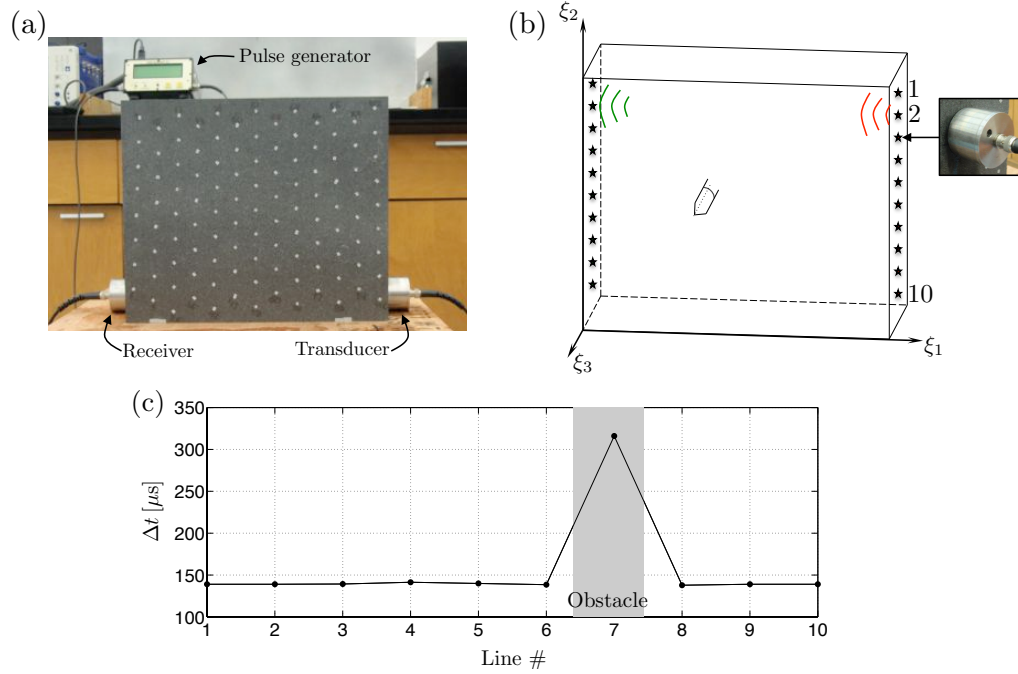


Figure 41: Ultrasonic time-of-flight measurements in Block-1 specimen.

# List of publications stemming from the project

## Published

1. R.D. Tokmashev, A. Tixier, and B.B. Guzina (2013). “Experimental validation of the topological sensitivity approach to elastic-wave imaging”, *Inverse Problems*, **29**, 125005 (25pp).
2. E.V. Dontsov, R.D. Tokmashev, and B.B. Guzina (2013). “A physical perspective of the length scales in gradient elasticity through the prism of wave dispersion”, *Int. J. Solids Struct.*, **50**, 3674-3684.

## In review

4. A. Wautier and B.B. Guzina (2013). “On the second-order homogenization of wave motion in periodic media”, 39pp.
5. B.B. Guzina and F. Pourahmadian (2014). “Why the inverse scattering by topological sensitivity may work”, 28 pp.

## In preparation

6. F. Pourahmadian and B.B. Guzina (2014). “On the elastic-wave sensing of fractures with interfacial stiffness”.
7. R.D. Tokmashev and B.B. Guzina (2014). “3D elastic-wave imaging of discrete damage in nuclear graphite from limited-aperture measurements”.

## References

- [1] ImageJ, image processing and analysis in Java, National Institute of Health. <http://imagej.nih.gov/ij>.
- [2] X-ray CT lab, university of minnesota. <http://xraylab.esci.umn.edu/sites/xraylab.esci.umn.edu>.
- [3] C. Bellis and M. Bonnet. A fem-based topological sensitivity approach for fast qualitative identification of buried cavities from elastodynamic overdetermined boundary data. *Int. J. Solids Struct.*, 47:1221–1242, 2010.
- [4] M. V. Berry and C. Upstill. Catastrophe optics: Morphologies of caustics and their diffraction patterns. *Progress in Optics*, 18:257–346, 1980.
- [5] N. Bleistein and R. A. Handelsman. *Asymptotic Expansions of Integrals*. Dover Publication, New York, 1986.
- [6] V. A. Borovikov. *Uniform Stationary Phase Method*. Instit. Electrical Engineers, London, 1994.
- [7] A. Carpio and M. L. Rapun. Topological derivatives for shape reconstruction. *Lect. Not. Math.*, 1943:85–131, 2008.
- [8] B. Cockburn and G. Karniadakis. *Discontinuous Galerkin methods: Theory, computation, and applications*. Springer, 2000.
- [9] D. Colton and R. Kress. *Inverse Acoustic and Electromagnetic Scattering Theory*. Springer-Verlag, New York, 1998.
- [10] E. V. Donstov, Tokmashev R. D., and Guzina B. B. A physical perspective of the length scales in gradient elasticity through the prism of wave dispersion. *Int. J. Solids Struct.*, 50:3674–3684, 2013.
- [11] G. R. Feijoo. A new method in inverse scattering based on the topological derivative. *Inverse Problems*, 20:1819–1840, 2004.
- [12] B. B. Guzina and M. Bonnet. Topological derivative for the inverse scattering of elastic waves. *Quart. J. Mech. Appl. Math.*, 57:161–179, 2004.
- [13] B. B. Guzina and M. Bonnet. Small-inclusion asymptotic of misfit functionals for inverse problems in acoustics. *Inverse Problems*, 22:1761–1785, 2006.
- [14] B. B. Guzina and F. Pourahmadian. Why the inverse scattering by topological sensitivity may work. *Proc. Royal Society A*, under review, 2014.
- [15] S. Ham and K. J. Bathe. A finite element method enriched for wave propagation problems. *Computers and Struct.*, 94-95:1–12, 2012.
- [16] A. Idesman. Accurate time integration of linear elastodynamics problems. *CMES*, 71:111–148, 2011.
- [17] S. Jarkov, Y. Titarenko, and G. Churilov. Electron microscopy studies of fcc carbon particles. *Carbon*, 36:595–597, 1998.
- [18] L. Jiang and J. Rogers. Effects of spatial discretization on dispersion and spurious oscillations in elastic wave propagation. *Int. J. for Num. Methods in Eng.*, 29:1205–1218, 1990.
- [19] M. Kaser and M. Dumbser. An arbitrary high order discontinuous galerkin method of elastic waves on unstructured meshes. *Geophys. J. Int.*, 142, 2006.
- [20] H. Kolsky. *Stress Waves in Solids*. Dover, New York, 1963.
- [21] A. Logg, K.A. Mardal, and G. Wells. *Automated Solution of Differential Equations by the Finite Element Method: The FEniCS Book*. Springer, 2012.
- [22] J. Miklowitz and J.D. Achenbach. *Modern problems in elastic wave propagation*. John Wiley, 1978.
- [23] T. Poston and I. Stewart. *Catastrophe Theory and its Applications*. Pitman, London, 1981.

- [24] G. Sadaka. FreeFem++, a tool to solve PDEs numerically. Preprint, Université de Picardie Jules Verne, <http://arxiv.org/pdf/1205.1293.pdf>, 2012.
- [25] J. J. Stamnes. *Waves in Focal Regions*. Taylor & Francis, New York, 1986.
- [26] R. D. Tokmashev, Tixier A., and Guzina B. B. Experimental validation of the topological sensitivity approach to elastic-wave imaging. *Inverse Problems*, 29:125005, 2013.